

Technische Universität Ilmenau  
Institut für Physik

DISSERTATION  
ZUR ERLANGUNG DES AKADEMISCHEN GRADES  
DOCTOR RERUM NATURALIUM  
DER MATHEMATISCH-NATURWISSENSCHAFTLICHEN FAKULTÄT  
DER TECHNISCHEN UNIVERSITÄT ILMENAU

**Single-Atom Junctions  
and Novel Electron Confinement Mechanism  
on Pb(111)**

vorgelegt von  
Martin Müller  
geboren am 26.06.1989  
in Plauen

1. Gutachter: Prof. Dr. Jörg Kröger
2. Gutachter: Prof. Dr. Stefan Krischok
3. Gutachter: Dr. Simon Crampin

Tag der Einreichung: 04.04.2017

Tag der wissenschaftlichen Aussprache: 31.08.2017

urn:nbn:de:gbv:ilm1-2017000352



# Abstract

Point contacts were established between the Pb covered tip of a Scanning Tunneling Microscope (STM) and a flat Pb(111) surface or single deposited Pb adatoms. The conductance was recorded while forming and subsequent breaking of these junctions. Contacts on the flat surface show a pronounced conductance hysteresis which is less prominent for contacts incorporating a single Pb adatom. The analysis of the experimentally recorded conductance and hysteresis width is supported by density functional calculations which reproduce the experimental findings. In order to fully reproduce the experimental results it was necessary to include tip apices terminated by more than one atom which is an important finding considering the large influence of the tip on results obtained by scanning tunneling microscopy and spectroscopy.

The second part of this thesis will present a study of a novel form of electron quantum confinement above Ar-filled nanocavities buried underneath a Pb(111) surface. The cavities are created by irradiation of the surface with high energetic argon-ions and subsequent annealing. A vertical confinement between the cavity and the crystal surface leads to quantum well subbands which were probed by scanning tunneling spectroscopy. The volume above the cavity can approximately be considered as a thin film with a finite lateral dimension. Unexpectedly the electrons are additionally laterally confined by the interface where the thin film recovers its bulk thickness. This lateral confinement leads to a fine structure in spectra of the differential conductance. The experimental findings will be supported by calculations based on the free electron gas which reproduce the results to a high degree. The lateral confinement is furthermore observable by a distinct standing wave pattern which was used to extract the dispersion relation of thin Pb film quantum well states in a range up to 2 eV. An analysis of the line widths of the spectroscopic features will reveal the influence of the interface of the thin film on the elastic decay rate.





# Zusammenfassung

Punktkontakte wurden zwischen der bleibedeckten Spitze eines Rastertunnelmikroskops und der flachen Pb(111) Oberfläche oder einzelnen Pb-Adatomen hergestellt. Der Leitwert wurde während des Aufbaus und des sich anschließenden Abbruchs des Kontakts aufgenommen. Kontakte auf der flachen Oberfläche zeigen eine starke Leitwerthysterese, die bei Kontakten mit einem einzelnen Pb-Adatom geringer ausgeprägt ist. Die Auswertung der experimentell aufgenommenen Kontaktleitwerte und Hysteresebreiten wird von Dichtefunktionalberechnungen unterstützt. Für eine vollständige Reproduktion war es notwendig, Spitzenapizes in Betracht zu ziehen, die von mehr als einem Atom terminiert werden. Dies ist ein wichtiges Ergebnis, wenn man den großen Einfluss der Spitze auf Ergebnisse der Rastertunnelmikroskopie- und Spektroskopie bedenkt.

Der zweite Teil dieser Arbeit wird sich mit einer neuartigen Form des Quanteneinschlusses von Elektronen beschäftigen, der über vergrabenen Nanokavitäten unter einer Pb(111)-Oberfläche beobachtet werden kann. Die Kavitäten werden durch den Beschuss der Oberfläche mit hochenergetischen Argon-Ionen sowie einem sich anschließenden Heizzyklus erzeugt. Ein vertikaler Einschluss von Elektronen zwischen der Kavität und der Oberfläche des Kristalls führt zu Quantentrogsubbändern, die mit Hilfe der Rastertunnelspektroskopie untersucht wurden. Das Volumen oberhalb der Vakanz kann näherungsweise als dünner Film mit begrenzter lateraler Ausdehnung angesehen werden. Überraschenderweise sind die Elektronen zusätzlich lateral eingeschlossen von der Grenzfläche, an der der dünne Film in das ungestörte Kristallvolumen übergeht. Diese laterale Beschränkung führt zu einer Feinstruktur, die in Spektren des differentiellen Leitwerts beobachtet werden kann. Die experimentellen Befunde werden durch auf dem freien Elektronengas beruhenden Berechnungen unterstützt, die die Ergebnisse zu einem hohen Grad reproduzieren. Die laterale Beschränkung drückt sich weiterhin durch ein charakteristisches stehende Welle

Muster aus, das genutzt wurde, um die Dispersionsrelation der Quantenzustände dünner Bleifilme in einem Bereich von bis zu 2 eV zu ermitteln. Eine Analyse der Linienbreite der spektroskopischen Charakteristika wird den Einfluss der Grenzfläche des dünnen Films auf die elastische Abklingrate zeigen.

# Contents

<b>1</b>	<b>Introduction</b>	<b>1</b>
<b>2</b>	<b>Scanning Tunneling Microscopy</b>	<b>5</b>
2.1	Basic Working Principle . . . . .	5
2.2	1D Square Potential Barrier . . . . .	6
2.3	The Tunneling Process in STM . . . . .	8
2.4	Operating Modes of STM and STS . . . . .	14
2.4.1	Surface Mapping . . . . .	14
2.4.2	Spectroscopy . . . . .	15
2.5	Experimental Setup . . . . .	16
2.5.1	UHV System . . . . .	16
2.5.2	Scanning Tunneling Microscope . . . . .	19
<b>3</b>	<b>Plasticity of Single-Atom Pb Junctions</b>	<b>21</b>
3.1	Introduction . . . . .	21
3.2	Experiment . . . . .	24
3.3	Results and Discussion . . . . .	25
3.4	Conclusion . . . . .	36
<b>4</b>	<b>Quantum Confinement above Nanocavities at Pb(111)</b>	<b>37</b>
4.1	Introduction . . . . .	37
4.2	Experiment . . . . .	39
4.3	Results and Discussion . . . . .	40
4.3.1	Spectroscopic Signatures . . . . .	40
4.3.2	Line Widths . . . . .	47
4.3.3	Quantum Well State Dispersion . . . . .	48
4.4	Conclusion . . . . .	52
<b>5</b>	<b>Summary and Outlook</b>	<b>53</b>
<b>A</b>	<b>Quantum Confinement</b>	<b>55</b>
	<b>List of Figures</b>	<b>59</b>

<b>Bibliography</b>	<b>67</b>
<b>List of the Author's Publications</b>	<b>79</b>
<b>Erklärung</b>	<b>81</b>
<b>Wissenschaftlicher Lebenslauf</b>	<b>83</b>
<b>Danksagung</b>	<b>85</b>

# 1 Introduction

“God made the bulk; surfaces were invented by the devil.” This quote was made by Wolfgang Pauli and is representative for the challenges faced in surface science. The breaking of the bulk symmetry completely alters the physical properties of surfaces and interfaces and is exploited in a wide variety of applications.

These challenges did not prevent the scientific community from further investigations, in contrast it induced the development of new experimental techniques which continuously improved over the last decades. The ongoing research gives us a deep understanding of e. g. catalysis, friction and electronic properties at the nanoscale. In particular, the tunable resistance and elastic properties of electric contacts containing only a single atom at the point of the smallest constriction may allow the development of electronic devices which finally reach the ultimate size limit.

The development of electronic circuits follows a roadmap (ITRS) predicting a 10 nm-process for 2017 which will be followed by 7 nm and 5 nm processes in 2018 and 2020 respectively. This means that in the foreseeable future the half-distance between identical features in an array of electronic circuits will decrease down to 5 nm. Due to the continuous miniaturization towards sizes comparable with interatomic distances the fundamental understanding of the physical properties in such scales is of crucial importance. The ultimate size limit for electronic circuits is the single atomic contact, which is hence a matter of current research. At such scales the consideration of the wave nature of the electrons is necessary for a complete description and macroscopic laws, like the Ohm’s law lose their applicability. The conductance of an atom sized contact becomes independent of its length and instead the electrons travel ballistically through the constriction. As a consequence the fundamental understanding of single-atomic contacts is a requisite for the future development of electronic

circuits. In this thesis a study of the electronic and mechanical properties of Pb contacts reaching the ultimate size limit is reported. Pb was chosen because it shows an increased conductance in nano contacts compared to other metals. For example, in macroscopic junctions Au has an order of magnitude higher conductance than Pb. This situation drastically changes when the junction comprises only a single atom and Pb conducts current  $\approx 2.5$  times better than Au. In addition it has been shown that the electronic transport properties strongly depend on the actual junction geometry and arrangement of the contributing atoms. Although a wealth of works has been reported in this field, experiments with highly controlled junction geometries are rare and more work is necessary for a fundamental understanding. Furthermore in this thesis not only the electronic but also the mechanical properties of nano junctions are investigated. The understanding of the elastic and inelastic effects during the opening and closing of contacts comprising only a small number of atoms may be of high interest for possible applications in the future.

Another part of this thesis will present a novel way of quantum confinement which can be observed atop buried cavities in a Pb crystal. Confinement of electrons to dimensions close to their fermi wavelength leads to a quantization of the electronic energies which in turn influences the physical properties of the material. This interplay of geometry and physical properties is exploited in a wide variety of applications, e. g. involving semiconductor hetero structures, novel catalytic materials and optoelectronics. The advancement of this field depends on the probing and characterization of new forms of quantum confinement. Thin films restrict electrons in a direction perpendicular to the surface resulting in the formation of so-called quantum well states. Thin Pb films in particular are attracting a considerable interest due to the possibility to grow them on wide range of different substrates and their strongly varying physical properties with film thickness. The fermi wavelength of Pb is approximately four times the interlayer spacing. This leads to an oscillation of the density of states at the fermi level with a bilayer periodicity which in turn influences the superconducting transition temperature, the surface energy, chemical reactivity and the electron phonon coupling. The properties of especially thin Pb films are well investigated and described in a wealth of works. An open question which still remains is the effect of the lateral dimension of the film, especially

---

when the thin-film is not restricted by a vacuum barrier but instead by an interface where the thin film recovers its bulk thickness. This is a hitherto unexplored confinement mechanism and may contribute to future applications in e. g. optoelectronics or catalysis.

The organization of the thesis is as follows. Chapter 2 will give an introduction into Scanning Tunneling Microscopy (STM). In a first step the basic working principle will be explained which will be followed by a brief recapitulation of the 1D potential barrier. Based on this simplistic description the tunneling problem in the context of STM will be summarized by introducing the most common models. The last two section will present the different measurement modes and the experimental setup.

Chapter 3 will provide an analysis of the electronic and mechanical properties of Pb nano contacts. For this purpose the tip of a STM was used to contact the flat Pb(111) surface as well as single deposited Pb adatoms. This procedure allows for a highly reproducible contact geometry. The  $I(z)$  characteristics were recorded during the approach and the retraction of the tip and show a hysteretic behavior. In combination with state-of-the-art density functional calculations the experimental results allow conclusions to be drawn about the elastic and inelastic properties as well as the atomic configuration of the contact.

Chapter 4 will present a study describing a novel form of quantum confinement which can be observed in the volume above buried nanocavities. Here the electrons are confined laterally by the interface between a thin film and the bulk of the crystal. The chapter will present the experimental findings and introduce a theoretical model based on the free electron gas.

Some of the chapters have been published in part or completely in peer reviewed journals:

- Chapter 3 has been published as *Plasticity of single-atom Pb junctions* by M. Müller, C. Salgado, N. Néel, J. J. Palacios, and J. Kröger in Phys. Rev. B **93**, 235402 (2016).
- Chapter 4 has been published in parts as *Lateral Electron Confinement with Open Boundaries: Quantum Well States above Nanocavities at Pb(111)* by M. Müller, N. Néel, S. Crampin and J. Kröger in Phys. Rev. Lett. **117**, 136803 (2016).





## 2 Scanning Tunneling Microscopy

The Scanning Tunneling Microscop (STM) has been developed by G. Binnig, H. Rohrer, Ch. Gerber and E. Weibel in the early 1980's [1, 2] and has since developed to a widely used tool in surface science. The STM is based on the quantum-mechanical tunneling effect which describes the possibility for electrons to penetrate classically forbidden regions in which the electron energy  $E$  is smaller than potential barrier height  $V$ .

The first section 2.1 describes the basic working principle and will be followed by section 2.2 describing the effects observed when an electron tunnels through a 1D rectangular potential barrier. This simple model already captures the fundamental properties of the STM. A more sophisticated model based on the works by Bardeen, Tersoff and Hamann which also describes the effects observed by scanning tunneling spectroscopy is presented in section 2.3 [3–5]. Sections 2.4 and 2.5 will give an introduction in the different operation modes utilized in this thesis and present the experimental setup.

### 2.1 Basic Working Principle

Figure 2.1 shows schematically the basic working principle of STM. In order to record a tunneling current a bias is applied and an atomically sharp tip is brought close to the sample. The approach to the sample is achieved with the help of piezo stacks using the slip-stick technique. After each coarse step the tube piezo of the scanner tests whether a tunneling current can be detected in its working range. This process is repeated until stable tunneling conditions are achieved.

Once a tunneling current can be recorded a feedback loop keeps the current at a certain setpoint by regulating the voltage applied to the z-piezo. Typical voltages applied between the tip and the sample range from several  $\mu\text{V}$  to some

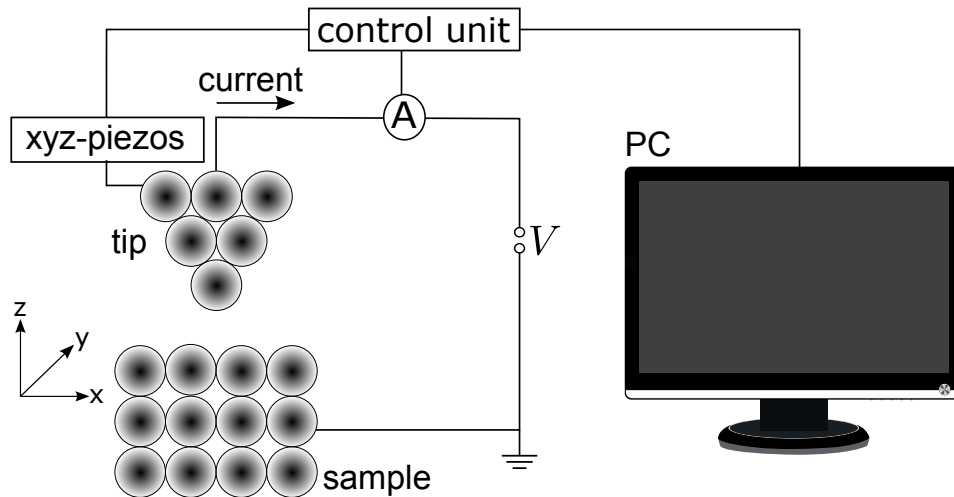


Figure 2.1: Schematic working principle of STM. The tip is brought in vicinity to the sample and a bias  $V$  is applied. The resulting tunneling current is amplified and recorded by the STM control unit. The control unit applies the high voltages to the x-, y- and z-piezos and controls the movement of the tip. During the scan the current is held constant by a feedback loop controlling the z-position of the tip.

$V$  whereas the current ranges from pA to several hundreds of nA. High-precision positioning parallel to the surface is achieved via piezo controlled movement of the tip. The most common STM operation mode is the so-called constant current scan. Here the current is held constant by the feedback loop and the tip scans across the surface. This operation mode allows the acquisition of a three-dimensional image of the surface and reduces the risk of an undesired contact between the tip and the sample. The spatially resolved z-position of the tip contains information about the topography as well as the electronic structure of the surface. For low voltages the recorded images can be interpreted in terms of contours of constant density of states (DOS).

## 2.2 1D Square Potential Barrier

The 1D square potential barrier is the simplest approach to describe the tunneling barrier in STM experiments. Despite its simplifications the obtained results are in good qualitative agreement with the experiment. The potential

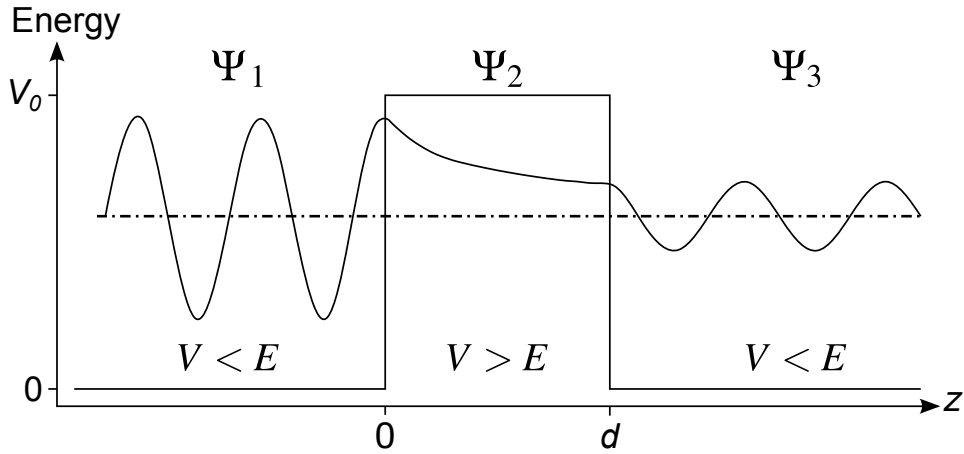


Figure 2.2: 1D square potential barrier with height  $V_0$  and width  $d$  and schematic wave function  $\Psi$  representing the quantum mechanical tunneling process. The wave function inside the barrier decays exponentially and is transmitted with a finite probability.

barrier is sketched in Figure 2.2 with height  $V_0$  and width  $d$ . The stationary Schrödinger equation

$$\left(-\frac{\hbar}{2m} \frac{d^2}{dz^2} + V(z)\right) \Psi(z) = E\Psi(z) \quad (2.1)$$

can be solved for an incoming wave with an amplitude of one moving from left to right (+) for all regions by three different wave functions

$$\Psi_1(z) = e^{ikz} + A_- e^{-ikz} \quad z < 0 \quad (2.2)$$

$$\Psi_2(z) = B_+ e^{i\kappa z} + B_- e^{-i\kappa z} \quad 0 < z < d \quad (2.3)$$

$$\Psi_3(z) = C_+ e^{ikz} \quad z > d \quad (2.4)$$

with the wave numbers

$$k = \sqrt{\frac{2mE}{\hbar^2}} \quad \text{and} \quad (2.5)$$

$$\kappa = \sqrt{\frac{2m(E - V_0)}{\hbar^2}} \quad . \quad (2.6)$$

The coefficients  $A_-$ ,  $B_+$ ,  $B_-$  and  $C_+$  can be derived from the boundary conditions at  $z = 0$  and  $z = d$ . The wave function  $\Psi$  and its derivative  $\Psi'$  have

to be continuous. From these coefficients the probability  $T$  for an electron to be transmitted through the barrier can be calculated.

$$T = |C_+|^2 \quad (2.7)$$

$$= \frac{1}{1 + \frac{V_0^2 \sinh^2(\kappa d)}{4E(V_0 - E)}} \quad (2.8)$$

For strong potentials ( $\kappa d \gg 1$ ) equation (2.8) can be approximated with an exponential relationship.

$$T \approx \left( \frac{4k\kappa}{k^2 + \kappa^2} \right)^2 e^{-2\kappa d} \quad (2.9)$$

For typical potential heights of 4-5 eV and barrier widths of several Ångström the transmission probability changes by one order of magnitude for a variation of 1 Å in the barrier width. This ballpark estimate explains the high spatial resolution achieved with STM.

## 2.3 The Tunneling Process in STM

The tunneling process in a STM can be described as an interaction between two independent electrodes, namely tip and sample [5–8]. Figure 2.3 shows the energy diagram of an STM setup.

In a biased junction tip and sample are separated by a trapezoidal energy barrier whose shape is determined by the work functions of tip  $\Phi_s$  and sample  $\Phi_t$ . The electron wave functions of both electrodes decay into the vacuum and overlap with the wave function of the counter electrode. These overlaps result in two electron currents flowing between tip and sample in both directions (see section 2.2). In an unbiased junction these two currents exactly cancel each other and the resulting net current is zero. In figure 2.3 a positive bias  $V$  is applied to the sample and the electrons can tunnel from occupied (light grey) tip states to unoccupied sample states leading to a net current from tip to sample. In the 1960's Bardeen proposed a theory based on Fermi's golden rule

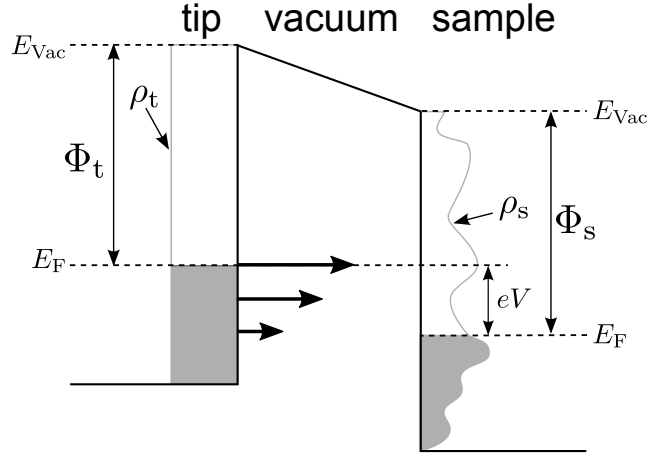


Figure 2.3: Tunneling process in STM for finite bias voltages. Tip and sample are separated by a vacuum energy barrier with a trapezoidal shape determined by the work functions  $\Phi_t$  and  $\Phi_s$  of tip and sample, respectively. With a positive voltage applied to the sample, the fermi levels  $E_F$  of tip and sample shift relative to each other and electrons tunnel from occupied tip states (light grey) to unoccupied sample states. The DOS of the tip  $\rho_t$  is set constant. The arrows indicate the direction of the flowing net current with the length of the arrows symbolizing the relative contributions. With higher energy the transmission probability of the electrons and their impact on the tunneling current increases.

describing the tunneling between to electrodes [5–8]. In this formalism the tunneling current for finite bias can be written as

$$I = \frac{4\pi e}{\hbar} \int_{-\infty}^{\infty} [f(E_F - eV + \varepsilon) - f(E_F + \varepsilon)] \times \rho_t(E_F - eV + \varepsilon) \rho_s(E_F + \varepsilon) |M_{ts}|^2 d\varepsilon \quad (2.10)$$

where  $\rho_s$  and  $\rho_t$  denote the local density of states of sample and tip, respectively. The fermi function  $f(E)$  accounts for the thermal broadening. The squared tunneling matrix elements  $|M_{ts}|^2$  describes the transmission probability  $T$  for electrons being transmitted through the barrier and can be expressed for an arbitrary barrier  $U(s)$  of width  $z$  with the well-known WKB expression [9, 10]

$$T = |M_{ts}|^2 = \exp \left[ -\frac{2}{\hbar} \int_0^z \sqrt{2m(U(s) - E)} ds \right] \quad (2.11)$$

with  $E$  denoting the energy of the electrons. For a trapezoidal barrier as shown in figure 2.3 the equation can further be simplified to

$$T(z, V, E) = \exp \left[ -2z \sqrt{\frac{2m}{\hbar^2} \left( \frac{\Phi_t + \Phi_s}{2} + \frac{eV}{2} - E \right)} \right] . \quad (2.12)$$

This relation reproduces the exponential dependency found for the 1D square potential from equation (2.9). At 0 K the fermi function simplifies to a step function and equation (2.10) can be written as

$$I = \frac{4\pi e}{\hbar} \int_0^{eV} \rho_t(E_F - eV + \varepsilon) \rho_s(E_F + \varepsilon) |M_{ts}|^2 d\varepsilon . \quad (2.13)$$

The majority of STM experiments is geared towards the investigation of the sample DOS  $\rho_s$  while the tip DOS  $\rho_t$  is typically unknown and it has become common practice, supported by experimental evidence, to assume a constant or only slowly varying DOS of the tip in the investigated energy range  $eV$ . The differential conductance can then be approximated by differentiating equation (2.13) with respect to  $V$  and yields [3, 4]

$$\frac{dI}{dV} = \frac{4\pi e^2}{\hbar} \rho_t(E_F) \rho_s(E_F + eV) T . \quad (2.14)$$

This is an important result and shows that I–V-characteristics measured by STM allow the direct probing of the local density of states of the sample. Combined with the possibility of the high accuracy positioning of the tip the STM provides means to study the electronic properties of a surface with sub-atomic resolution. It is important to note that a crucial requirement for the validity of equation (2.14) is a constant tip DOS meaning that  $d\rho_t/dV = 0$  for the investigated energy range. A commonly utilized technique to assure a constant tip DOS is the covering of the tip with substrate material by intending it into the substrate [11]. A subsequent investigation of a surface with a well-known electronic structure, like a noble-metal substrate, by scanning tunneling spectroscopy (STS) allows conclusions to be drawn about features in the tip DOS which may influence the recorded spectra. An absence of such features

is absolutely necessary for a reliable and reproducible interpretation of the recorded I–V-characteristics.

Additionally equation (2.14) requires a constant transmission probability  $T$ . While this is a good approximation for energies  $eV$  close to zero, the exponential dependence has to be taken in consideration for elevated voltages. Starting at equation (2.13) reference [12] derives the sample density of states considering a non-constant transmission factor:

$$\rho_s = \frac{1}{eT[z(V), V, eV]} \left\{ \frac{dI}{dV}[z(V), V] + \frac{e\sqrt{2m}z(V)}{2\hbar\sqrt{\Phi}} I \right\} \quad (2.15)$$

Here  $\Phi = \frac{\Phi_s + \Phi_t}{2}$  is the effective barrier height and  $z(V)$  denotes the absolute distance between tip and sample. While the absolute distance is typically not known the variation of tip excursion  $\Delta z$  relative to a certain offset value  $z_0$  is routinely recorded simultaneously to the  $I(V)$  and  $dI/dV(V)$  signals. The absolute distance can then be approximated by  $z = z_0 + \Delta z$ . Reference [12] shows that  $z_0$  does not drastically influence the spectral line shape if varied in a range which is common for STM experiments. Equation (2.15) allows to eliminate the influence of the transmission factor and provides means to link the  $dI/dV$  signal and the sample density of states for large applied voltages and non-constant tip–sample separation distances. The procedure of applying equation (2.15) to an recorded  $dI/dV$ -spectra is often referred to as a so-called normalization. An example of such a normalization is provided in figure 2.4(a). The spectra is showing the spectroscopic signature of the highest occupied quantum well state of a Pb thin-film atop a buried cavity of which a detailed analysis will provided later in this thesis. The black curve represents the recorded and unmodified  $dI/dV$  signal. The red curve is computed by applying (2.15) to the unmodified spectra, i. e. by normalizing it. In the unmodified spectra the influence of the transmission factor on the spectroscopic signature is clearly visible in form of an exponential background. After the normalization this exponential influence is strongly decreased and the spectra now resembles the theoretically expected density of states (see chapter 4).

To record the differential conductance in constant height mode, the tip is positioned atop the desired sample position and the feedback loop is opened

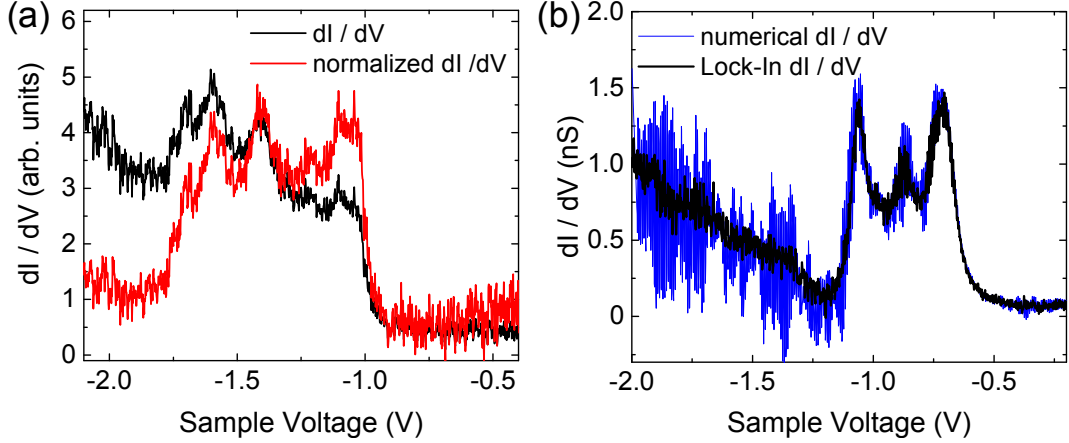


Figure 2.4: (a) Comparison between a unmodified (black) and a normalized (red) constant-height  $dI/dV$ -spectra showing the HOQWS of a Pb thin-film atop a buried cavity. The normalization was achieved by applying equation (2.15) to the unmodified spectra with the parameters  $\Phi = 4.2$  eV and  $z_0 = 1$  nm. The feedback loop was opened at  $V = -2.5$  V and  $I = 0.5$  nA. (b) Comparison between a  $dI/dV$ -spectra obtained by the numerical differentiation of the  $I(V)$ -curve (blue) and the same unmodified  $dI/dV$ -spectra obtained by Lock-In-technique (black). The feedback loop was opened at  $V = -2$  V and  $I = 0.5$  nA.

at a certain setpoint  $V_{\text{set}}$  and  $I_{\text{set}}$ . The current is recorded while the voltage is ramped through the energy range of interest. The easiest way to obtain the differential conductance is to compute a numerical differentiation of the  $I(V)$  signal which is shown as a blue curve in figure 2.4(b). The numerical derivative only yields a very poor signal to noise ratio (SNR) which is insufficient for most experiments. A common utilized method to increase the SNR is the so-called Lock-In technique [13]. Here a small high-frequency modulation bias  $V_{\text{mod}} \sin(\omega t)$  is superimposed to the applied sample voltage which in turn causes an answer in the current. If the modulation amplitude  $V_{\text{mod}}$  is much smaller than the bias voltage  $V_{\text{bias}}$ , the modulated current can be expanded in a Taylor series:

$$\begin{aligned}
 I[V_{\text{bias}} + V_{\text{mod}} \sin(\omega t)] &\approx \\
 I(V_{\text{bias}}) + \frac{dI(V_{\text{bias}})}{dV} V_{\text{mod}} \sin(\omega t) + \frac{d^2 I(V_{\text{bias}})}{dV^2} V_{\text{mod}}^2 \sin^2(\omega t) + \dots
 \end{aligned}
 \tag{2.16}$$

The first term is the unmodulated direct current. The second term is the first harmonic of the current response and has an amplitude which is proportional



to the differential conductance signal. By means of a Lock-In amplifier it is now possible to record the  $dI/dV$ -signal by mixing the response signal with a reference signal oscillating at the same frequency as the voltage modulation. Multiplying the response signal from equation (2.16) with a sinusoidal phase shifted reference signal  $\sin(\omega t + \varphi)$  yields:

$$I_{\text{out}} \propto \sin(\omega t + \varphi) \left[ I(V_{\text{bias}}) + \frac{dI(V_{\text{bias}})}{dV} V_{\text{mod}} \sin(\omega t) + \dots \right] \quad (2.17)$$

$$= \underbrace{\sin(\omega t + \varphi) I(V_{\text{bias}})}_{\text{AC}} + \frac{1}{2} \frac{dI(V_{\text{bias}})}{dV} V_{\text{mod}} \left[ \underbrace{-\cos(2\omega t + \varphi)}_{\text{AC}} + \underbrace{\cos(\varphi)}_{\text{DC}} \right] + \dots \quad (2.18)$$

The output contains AC and DC components. After eliminating the AC components with a low-pass filter only the DC component remains which is directly proportional to the differential conductance and only depends on the phase difference  $\varphi$  between reference and response signal. The DC component is then outputted by the Lock-In amplifier and can be recorded parallel to the  $I(V)$ -signal. To obtain the highest possible output signal the phase difference  $\varphi$  should be close to zero. With this detour the Lock-In technique is able to strongly increase the SNR by effectively suppressing broad-band noise. Only frequencies close to the modulation frequency can pass the low-pass filter and it is therefore of crucial importance to choose a modulation frequency which is not in resonance with electronic or mechanical noise of the experimental setup. In figure 2.4(b) the significant improvement in the SNR using the Lock-In technique (black curve) compared to a numerical derivative (blue curve) is clearly visible.

The STM provides furthermore direct access to the effective work function of the electrodes by studying the exponential behavior between tunneling current and tip excursion  $z$ . For voltages close to zero the tunneling current from equations (2.12) and (2.13) can be approximated by

$$I = \frac{4\pi e}{\hbar} V \rho_s(E_F) \rho_t(E_F) \exp\left(\frac{2z}{\hbar} \sqrt{2m\Phi}\right) \quad (2.19)$$

$$I \propto \exp(-1.025 \sqrt{\text{eV}^{-1} \text{\AA}^{-1}} \sqrt{\Phi} z) \quad (2.20)$$

with  $\Phi = \frac{\Phi_s + \Phi_t}{2}$  being the effective barrier height. If the current is plotted logarithmically the effective barrier height can directly be calculated from the slope of  $\ln(I(z))$  [7]

$$\Phi = \frac{\hbar^2}{8m} \left( \frac{d \ln I}{dz} \right) . \quad (2.21)$$

## 2.4 Operating Modes of STM and STS

### 2.4.1 Surface Mapping

#### Constant Current Topography Scan

In the constant current topography scan mode the current is held constant at a certain sample voltage by a feedback loop which adjusts the vertical tip excursion during the scan. The scan is performed line by line and the topography, i. e. the tip displacement, can be recorded during the forward as well as the backward scan. A typical topography scan therefore leads to two images of the surface which can be utilized for quality control purposes. If the same surface feature appears differently in the forward and backward scan, it is in the most cases a sign for a too slowly regulating feedback loop or a highly asymmetric tip apex. To avoid artifacts in the topography scans an ideally monoatomic tip apex and a well-tuned feedback loop are of uttermost importance. For low voltages a constant current topography map can be considered a contour of constant integrated local density of states (see equation (2.13)). The 3D contour of the tip displacement therefore contains information about the electronic structure as well as the actual topography of the surface.

#### Constant Current $dI/dV$ Scan

The  $dI/dV$  mapping mode offers the possibility to record the LDOS at a given energy  $eV$ . Similar to the constant current topography scan the current is held constant by the feedback loop at a given sample voltage. In this scanning mode the  $dI/dV$ -signal is recorded simultaneously to the topography. The  $dI/dV$ -signal is directly related to the LDOS at energy  $eV$  and equation (2.15) can be used to normalize the recorded  $dI/dV$ -map. For low voltages and small

tip displacements relative to the tip-sample separation it is commonly assumed, backed up by experimental evidence, that the constant current  $dI/dV$ -map is directly proportional to the LDOS without the application of any normalization.  $dI/dV$ -maps allow direct experimental access to e. g. the chemical substructure of molecules or like in the case of this thesis the real space mapping of confined electronic states. Note that the modulation frequency has to exceed the cut-off frequency of the feedback-loop to avoid a continuous adjusting of the tip in resonance with the modulation. The scan speed has to be reduced compared to the constant current topography scan to account for the averaging time necessary to achieve a sufficient SNR.

## 2.4.2 Spectroscopy

### Constant Height $dI/dV$ Spectroscopy

This spectroscopy mode allows the acquisition of the LDOS at a fixed point of the surface for an extended energy range. After the tip is positioned at the desired location the feedback loop is disabled and the voltage is ramped through the energy range of interest while the current and the  $dI/dV$ -signal are recorded. In constant height mode the energy range which can be covered by a single spectra is limited by the exponential energy dependence of the current (see equation (2.12)). If the energy range is chosen too large, parts of the spectrum may show an insufficient SNR or an intensity which exceeds the output specifications of the Lock-In amplifier.

### Constant Current $dI/dV$ Spectroscopy

In contrast to the constant height spectroscopy the feedback loop stays active for the constant current spectroscopy. While the voltage is ramped the tip displacement  $z(V)$  is adjusted to keep the current constant and the  $dI/dV$ -signal is recorded concomitantly. The active feedback loop again requires that the modulation frequency exceeds the cut-off frequency of the feedback loop to avoid a resonating oscillation of the tip. In this thesis the constant current spectroscopy is utilized to map wide energy ranges from 0.05 eV up to 10 eV in a single spectra which is not possible in constant height mode.

## **I(z) Spectroscopy**

$I(z)$  spectroscopy is a tool to investigate the effective work function as well as to perform conductance measurements in the contact regime. In order to perform  $I(z)$  spectroscopy the tip is moved to the desired position and the feedback loop is opened at a given sample voltage. Subsequently the tip is approached to the surface with an adjustable speed while the current is recorded. In the tunneling regime the  $I(z)$  dependence allows conclusions to be drawn about the effective work function following equation (2.21). After a certain tip displacement the tip and sample can be considered to be in contact (see chapter 3). In this contact regime the  $I(z)$  depends on the atomic configuration and the elastic properties of the electrodes.

## **2.5 Experimental Setup**

### **2.5.1 UHV System**

All experiments presented in this thesis were performed under ultra-high vacuum conditions (UHV). This is a necessary step to obtain well characterized atomically clean surfaces and to avoid contamination of the surface by residual gases. Additionally the STM is operated at ultra-low temperatures to improve the spectroscopic resolution and to reduce the mobility of adsorbents on the surface and the tip. In order to achieve these UHV and ultra-low temperature conditions a sophisticated experimental setup is necessary.

Figure 2.5 shows a photography of the UHV system which is a custom-built setup by *Createc Fischer & Co.* The system has two major parts, the analysis chamber on the left and the preparation chamber on the right. The differentially pumped manipulator allows the transfer of samples and tips between the two chambers as well as the positioning of the sample for preparation purposes. In order to sustain the UHV conditions the preparation chamber is equipped with a turbomolecular pump with a rotary vane roughening pump, an ion-getter pump and a titan sublimation pump. With this setup pressures below  $1 \cdot 10^{-10}$  mbar can be achieved. The whole UHV system is mounted on a stainless steel frame which rests on four laminar flow air dampers to decouple the chamber from

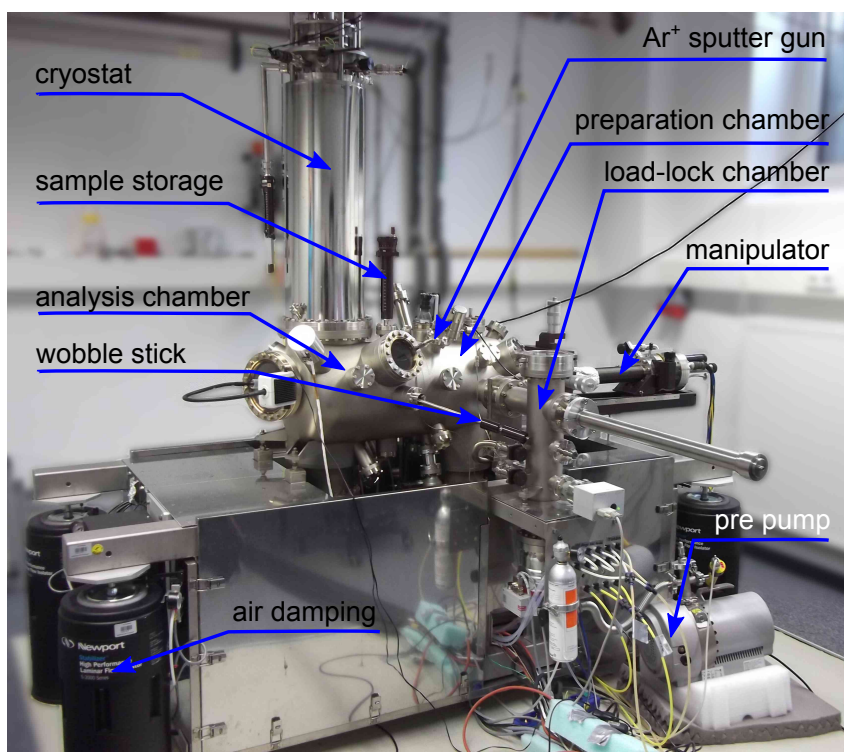


Figure 2.5: Photography of the experimental UHV setup. The most important parts are labeled. The setup consists of two separated chambers, the preparation chamber and the analysis chamber with the mounted cryostat. The load lock chamber allows to load samples into the UHV without breaking the vacuum of the preparation chamber.

the mechanical vibrations of the building. Additionally the dampers rest on a solid concrete block which is cut free from the foundation of the building.

The preparation chamber contains various tools for sample preparation. The manipulator is equipped with a filament mounted directly below the sample storage position which can be used for annealing. Sample temperatures up to 1000 K can be achieved by radiation heating. By applying an additional positive high voltage to the sample the temperature can further be increased up to 2800 K utilizing electron beam heating. The sample can furthermore be bombarded with high energetic argon ions, a process commonly known as argon sputtering. The argon gas is provided via a high precision leak valve. The preparation chamber also exhibits two electron beam evaporators for the deposition of high-melting metals and a quadrupole mass spectrometer to investigate the composition of the residual gases and to perform leak checks. In order to load samples and tips into the UHV without breaking the vacuum the chamber is equipped with a load lock. The load lock is separated from the preparation chamber by a gate valve and has an independent turbomolecular and roughening pump.

The analysis chamber is visible in the left part of the photography in figure 2.5 and is separated from the preparation chamber by a gate valve. The UHV conditions are ensured by an ion-getter pump and a titan sublimation pump. The analysis chamber is dominated by the liquid helium bath cryostat. In order to achieve cryogenic temperatures at the STM body and to reduce liquid helium consumption the cryostat consists of several differential cooling stages. The innermost part is filled with up to 10 l of liquid helium. The evaporating liquid helium cools an enclosing shield to approximately 20 K. The outermost stage consists of a 20 l liquid nitrogen bath at 77 K. The STM is mounted inside of a aluminum shield which fixed at the bottom of the liquid helium bath. This liquid helium shield is completely enclosed by an additional shield which is fixed at the bottom of the liquid nitrogen bath. With this setup a measurement temperature of about 6 K can be sustained for 72 hours without the need of refilling the cryostat. The wobble stick is used to transfer tips and samples between the sample storage, the STM and the manipulator.

During the measurement all mechanical pumps, i. e. the roughening as well as the turbomolecular pumps, are turned off and the UHV is maintained by

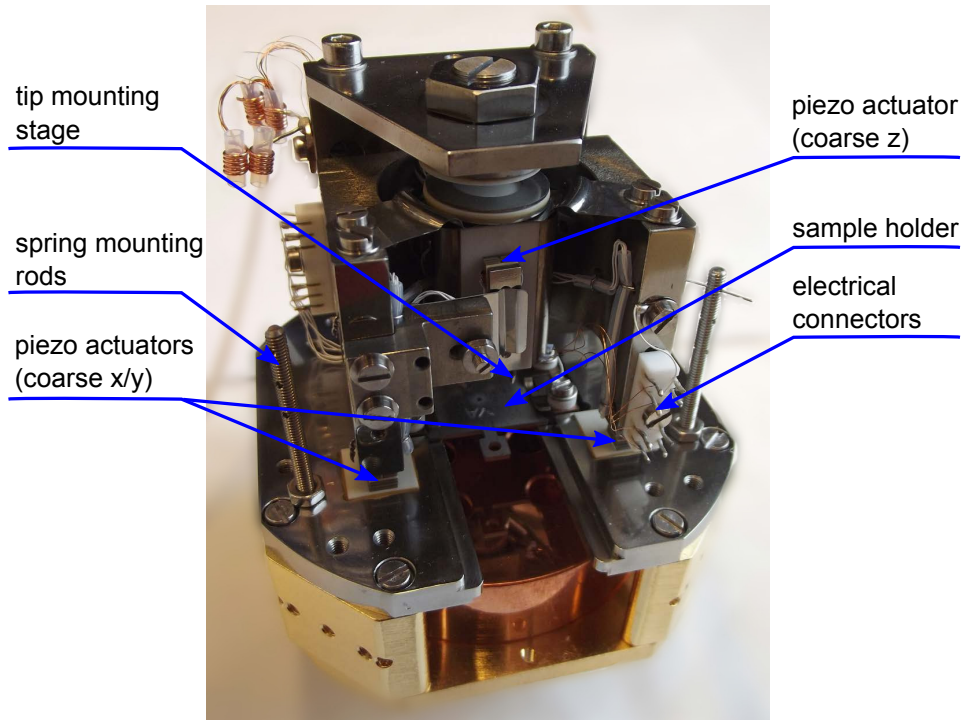


Figure 2.6: Photography of the unmounted STM body. The most important parts are labeled. During measurements the STM body is hanging spring-suspended from the bottom of the liquid helium cryostat.

the ion getter pumps. All separateable chamber parts contain an ionization gauge to monitor the pressure.

### 2.5.2 Scanning Tunneling Microscope

Figure 2.6 shows a photograph of the unmounted STM body. Inside of the UHV chamber the STM is spring-suspended from the bottom of the cryostat. The springs allow for an effective decoupling of the STM and the UHV chamber to decrease mechanical vibrations. The samples used in this thesis are hat-shaped with a bottom diameter of 8 mm, a top diameter of 5 mm and a thickness of 2 mm. The samples exhibit a roughness depth below  $0.01 \mu\text{m}$  and a miss-cut angle below  $0.4^\circ$ . The samples are fixed on an Omicron style sample holder with a shallow indentation corresponding to the bottom diameter of the hat-shape. Inside the STM the sample holder is fixed mechanically and the coarse as well as the fine positioning is carried out by tip.

The tip holder (not shown) is mechanically fixed by springs in the tip mounting stage which is placed at the bottom of a tube with a triangular cross-section. The fine positioning of the tip is achieved by a vertically mounted piezoelectric tube scanner. The piezo constants at 6 K are  $44 \text{ \AA/V}$  in x and y direction and  $10 \text{ \AA/V}$  in z direction. The coarse movement in z-direction is performed by a piezo stack which presses against the triangular tube (see figure 2.6). The whole tip setup rests on three feet standing on the ground plate of the STM body. These three feet contain piezo stacks which allow for a coarse positioning of the tip in x and y direction utilizing a stick-slip motion.

The STM is controlled by commercially available *Createc* electronics, high-voltage amplifiers and software. The current flowing through the tip is converted to a voltage by the transimpedance amplifier *Femto DLPCA-200* with a variable gain in the range between  $10^3 \text{ V/A}$  and  $10^{11} \text{ V/A}$ . The high voltage amplifier supplies voltages in range of  $\pm 300 \text{ V}$  which can be applied to the coarse movement piezos and the piezoelectric tube scanner. The STM electronics contain several 20 bit analog to digital (ADC) and digital to analog converters (DAC) which allow for high precision measurements. Lock-In measurements are performed by a *SR830* from *Stanford Research Systems* [14].



# 3 Plasticity of Single-Atom Pb Junctions

Reprinted (adapted) with permission from  
Phys. Rev. B **93**, 235402 (2016).  
Copyright 2016 American Physical Society.

A low-temperature scanning tunneling microscope was used to fabricate atomic contacts on Pb(111). Conductance characteristics of the junctions were simultaneously recorded with forming and subsequent breaking of the contacts. A pronounced hysteresis effect in conductance traces was observed from junctions comprising the clean Pb(111) surface. The hysteretic behavior was less profound in contacts to single Pb atoms adsorbed to Pb(111). Density functional calculations reproduced the experimental results by performing a full *ab initio* modeling of plastic junction deformations. A comprehensive description of the experimental findings was achieved by considering different atomic tip apex geometries.

## 3.1 Introduction

Electrical contacts with constrictions at the atomic scale are receiving substantial attention owing to their importance in fundamental and applied sciences. [15–17] In particular, molecular spintronics, [18] spin caloritronics [19] and thermoelectric effects in nanoscale junctions [20] are emerging fields. To these investigations structural and mechanical properties of the junctions are relevant since electron transport depends crucially on the contact geometry. [21, 22]

A wealth of experimental and theoretical works has been reported for Au contacts, [15] presumably due to their propensity to form monoatomic chains bridging the electrodes. [23, 24] By appropriate treatment of Au electrodes in break-junction experiments hysteretic loops were reproducibly observed in conductance-versus-distance traces that were simultaneously recorded with

closing and opening of the junctions. [25] This observation was traced to the elasticity of the electrodes. To our knowledge this work [25] represents the only combination of experimentally observed and theoretically described hysteretic conductance behavior between tunneling and contact range of single-atom junctions that has been available to date. Other materials that have often been used in contact experiments are Ni, Cu, Pd, Ag, Al and Pt. [15] For some of these materials conductance hysteresis upon opening high-conductance junctions were reported. [26–29]

For Pb contacts, which are the focus of this article the following experiments and calculations were reported. [15] In an early work W tips of a scanning tunneling microscope (STM) were approached to Pb(110) and neck formation was investigated at different sample temperatures. [30] Neck heights exceeding 500 nm were reported and their growth was rationalized in terms of mobile surface atoms. In another experiment polycrystalline Pb tips and samples were used to study the conductance of Pb junctions depending on the forces exerted on the electrodes. [26] A jump to contact was observed upon approaching the tip to the sample surface. The resulting junction conductance of less than one quantum of conductance,  $G_0 = 2e^2/h$  ( $e$ : elementary charge,  $h$ : Planck constant), was rationalized in terms of constrictions comprising about one atom. In addition, conductance hysteresis was reported after indenting the tip into the substrate, thereby increasing the junction conductance to  $\approx 10 G_0$ , and subsequent retraction of the tip. The contact area was appreciably modified by forming asperities with diameters on the order of 100 nm. In a break junction experiment Pb–Pb contacts were stretched until an abrupt decrease of the conductance occurred from  $\approx 1 - 3 G_0$  to typical tunneling conductances. [31] Tight-binding calculations assuming a simple pyramid-based geometry for the electrodes confirmed conductance values of  $\approx 2.5 G_0$  as a result of electron transport through  $sp_z$ ,  $p_x$ ,  $p_y$  orbitals of the Pb atom bridging the electrodes.

In the ballistic electron transport range, STM experiments revealed that contact formation between Pb-covered W tips and thin films of Pb on Ag(111) depended on the film thickness. [32] While a gradual transition from tunneling to contact was observed for the single Pb wetting layer, the transitions became more abrupt for thicker films. Conductances of contacts comprising the single Pb wetting layer as well as several layers were broadly distributed around

$\approx 2 G_0$ . For Pb(111) films on Si(111) atomically resolved conductance traces were obtained by using Pb-coated PtIr tips. [33] On-top, bridge, face-centered cubic and hexagonal close-packed sites of the Pb(111) lattice led to different conductances in the range of  $\approx 1 - 1.3 G_0$ .

Pb junctions were likewise investigated in electrochemical environments. [34] Accompanying density functional calculations revealed the importance of the contact geometry for the conductance. Also superconducting properties of Pb contacts exposed to external magnetic fields were demonstrated to depend on the junction geometry. [35] Moreover, atomic Pb wires were grown on a vicinal semiconductor surface and demonstrated to exhibit correlated spin-orbit order. [36] In tunneling junctions comprising Pb electrodes the competition of superconducting phenomena and Kondo screening [37] as well as tunneling processes into localized subgap states were unraveled. [38]

Here, we present a surface science approach to single-atom contacts fabricated from Pb-covered W tips and a Pb(111) surface in a low-temperature STM experiment. The forming and breaking of junctions was performed on pristine Pb(111) as well as on single Pb adsorbed atoms (adatoms). Simultaneously, the conductance of the junction was recorded for tip-sample distances in tunneling and contact ranges. Both types of junctions exhibited a rather broad distribution of contact conductances, *i. e.*, from  $1 G_0$  to  $5 G_0$  for Pb(111) and from  $0.7 G_0$  to  $3 G_0$  for Pb adatoms. These variations are not compatible with the previous tight-binding calculations for a single-atom Pb junction where conductance variations from  $1 G_0$  to  $2.5 G_0$  depending on the distance between the central atom and its first neighbors were reported. [39] In addition, both junctions showed hysteretic behavior. Breaking of the contacts on clean Pb(111) required tip retractions by up to hundreds of pm beyond the jump to contact. Contact regions were imaged prior to and after contact experiments in order to identify surface and tip modifications. The experimental results were corroborated by state-of-the-art *ab initio* quantum mechanical simulations. The calculations unveiled the important role of relaxations of the tip structure on the contact conductance and the hysteresis width. Atomically sharp and crystalline tips alone were unable to explain the experimental observations. Rather, tip apices terminated by more than one atom had additionally to be

considered to describe the experimentally observed contact conductances and hysteresis effects.

## 3.2 Experiment

The experiments were performed with an STM operated in ultrahigh vacuum ( $10^{-9}$  Pa). The absence of the superconducting energy gap in spectra of the differential conductance together with the temperature readings from a Si diode indicated a sample temperature of 7.2 K – 7.5 K. Pb(111) was cleaned by  $\text{Ar}^+$  bombardment and annealing. Tips were electrochemically etched from polycrystalline W wire (diameter  $300\ \mu\text{m}$ , purity 99.95 %) in a 0.1 M solution of NaOH. In the vacuum recipient the tips were heated close to the W melting temperature. The tip apex was then coated with substrate material by indentation into the Pb(111) surface with an applied voltage of 130 V.<sup>1</sup> A similar procedure was reported previously, which ensured the bulk-like character of the Pb coating by measuring the superconducting energy gap. [40] Tip–surface contacts were formed by disabling the feedback loop at a tunneling current of 0.5 nA, at a bias voltage between  $-50$  mV and 50 mV, and approaching the tip by 300–600 pm towards the surface. The tip approach was stopped a few tens of picometers after the first jump to contact. The tip was then retracted by 1 nm. Approach and retraction velocities ranged between  $2\ \text{nm s}^{-1}$  and  $3\ \text{nm s}^{-1}$ . For the contact experiments a specific selection of tips was used. The tip was approached to the surface until a single Pb atom was transferred from the tip to the sample upon contact. Atom transfer from the tip apex to the surface was reported previously for several surfaces [16, 17, 41–43] and is due to the strong adhesive forces between the electrodes close to the point of maximum attraction. Such tips were particularly stable and led to reproducible conductance traces and STM images prior to and after contact formation. STM images were recorded at constant current with the bias voltage applied to the sample. For measurements with a time resolution of 20 ns a transimpedance amplifier with a 3 dB cut-off frequency of 14 MHz and an oscilloscope sampling rate of  $50\ \text{MS s}^{-1}$  were used.

---

<sup>1</sup>Experiments were likewise performed with bulk Pb tips. The resulting junctions exhibited virtually identical behavior to the contacts with Pb-covered W tips.

### 3.3 Results and Discussion

Tip approach to the clean Pb(111) surface gave rise to the evolution of the junction conductance depicted as the black line in Fig. 3.1(a). The tunneling range in the vicinity of the transition to contact ( $-100 \text{ pm} < \Delta z < 0 \text{ pm}$ ) was characterized by an exponential increase of the conductance with an apparent barrier height of  $(5.0 \pm 0.5) \text{ eV}$ . This value is larger than the Pb(111) work function of  $4.05 \text{ eV}$ . [44] The deviation is in accordance with the previously reported increase of the apparent barrier height close to contact formation on thin Pb films on Ag(111). [32] Indeed, the calculations presented below revealed strong atomic relaxations in the vicinity of the tunneling-to-contact transition. Therefore the tip–surface distance decreased faster than the tip displacement, which is defined by a linear voltage ramp applied to the piezoelectric scanning unit.

The transition from the tunneling range to the contact range was reflected by an abrupt increase of the junction conductance. Time-resolved measurements of the jump to contact revealed that the transition was abrupt on a time scale of  $20 \text{ ns}$ . This almost discontinuous tunneling-to-contact transition was used to define  $\Delta z = 0 \text{ pm}$  [Fig. 3.1(a)]. These observations are compatible with the emerging trend reported previously. [32] While for a single wetting layer of Pb on Ag(111) the transition from the tunneling to the contact range was gradual, it turned into a more abrupt cross-over region for thicker Pb films. [32] Therefore, a jump to contact for bulk Pb may be expected and was observed in our experiments. The conductances just before [ $G_j$ , Fig. 3.1(a)] and after ( $G_c$ ) the jump did not depend on the applied bias voltage in the range of  $-50 \text{ mV}$  to  $50 \text{ mV}$ . Tunneling spectra of the differential conductance were featureless and nearly constant in that voltage interval.

In the subsequent contact range, *i. e.*, for  $\Delta z > 0 \text{ pm}$ , the conductance exhibited a linear increase. Upon tip retraction the junction conductance decreased linearly [gray line in Fig. 3.1(a)] several hundreds of pm beyond the precedent point of contact formation, *i. e.*, the conductance displayed a pronounced hysteretic behavior. The conductance decrease in the contact range ( $\Delta z < 0 \text{ pm}$ ) was reported previously and rationalized in terms of the splitting of Pb  $p$  orbitals at the Fermi level due to elastic distortions of the contact.[39]

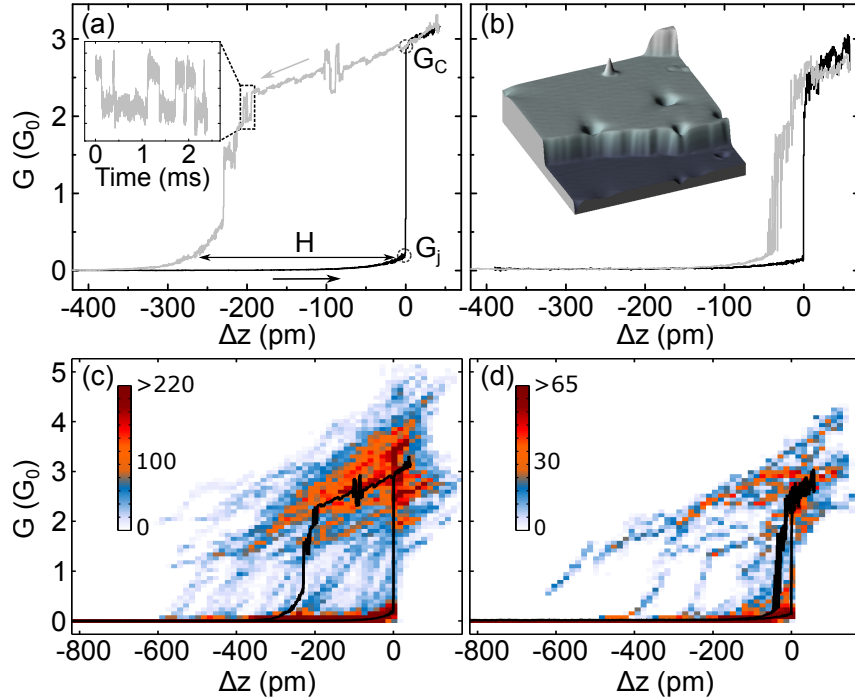


Figure 3.1: (a) Representative conductance evolution of a junction comprising Pb(111) and a Pb-coated W tip acquired at 50 mV. Tip approach (black line) leads to an exponential increase of the conductance in the tunneling range (displacements  $\Delta z < 0$  pm). The abrupt change of the conductance from  $G_j = 0.2 G_0$  to  $G_c = 2.9 G_0$  at  $\Delta z = 0$  pm reflects the formation of the contact. In the probed contact range ( $\Delta z > 0$  pm) the conductance increases linearly. Upon tip retraction (gray line) the conductance decreases linearly and reveals instabilities in the form of, *e. g.*, two-level fluctuations (dashed rectangle). The definition of the hysteresis width,  $H$ , is indicated. Inset: Two-level fluctuations observed in the conductance trace upon tip retraction. (b) Like (a) for a contact to a single Pb adatom on Pb(111) with  $G_j = 0.1 G_0$  and  $G_c = 2.2 G_0$ . Inset: Pseudo-three-dimensional representation of an STM image of Pb(111) (0.1 V, 55 pA, 50 nm  $\times$  50 nm). Two terraces are visible. A Pb adatom appears as a protrusion on the upper terrace. Additional structure is due to near-surface voids induced by  $\text{Ar}^+$  bombardment. [45, 46] Image processing was performed using WSxM. [47] (c), (d) Density plots of all acquired conductance traces [137 for Pb(111), 19 for single Pb adatoms]. The color scale depicts the number of conductance data linearly grouped into bins defined by a regular  $90 \times 90$  grid, which was spanned from  $-1090$  pm to  $260$  pm and from  $0 G_0$  to  $7 G_0$ . Full lines are the conductance traces shown in (a), (b). This figure was reproduced from [48] with permission from the American Physical Society.

During retraction of the tip two-level fluctuations of the conductance were often observed [dashed rectangle in Fig. 3.1(a)]. Data acquisition with high time resolution [inset to Fig. 3.1(a)] revealed that the fluctuations were abrupt changes between two conductance values, which may be attributed to atomic relaxations in the junction. [49–51] Local heating of the junction due to power dissipation in the  $\mu\text{W}$  range is likely to be present. For Au junctions a temperature increase of 50 mK was unraveled for this power dissipation. [52] On general grounds, in the case of electron and hole injection into pure metal a temperature increase on the order of 1 mK may be estimated for the used currents and bias voltages assuming that electrons and holes deposit their energy within the inelastic mean free path. [53] This temperature increase is not sufficient to surpass Ehrlich-Schwoebel barriers (86 meV) [54] and kink energies per atom (61–87 meV) [55] of Pb(111). Therefore, local heating of the junction does not represent the main driving mechanism for the observed junction instabilities. Importantly, after acquiring a typical conductance trace on Pb(111) [Fig. 3.1(a)] STM images of the contact area showed that in most cases a single atom was transferred from the tip to the surfaces. In less frequent cases a Pb dimer was transferred.

Contact experiments on single Pb adatoms were likewise performed. Single Pb atoms were transferred from the tip to the Pb(111) surface, as reported previously for other surfaces. [16, 17, 41–43] The inset to Fig. 3.1(b) shows an STM image of Pb(111) where a single adatom is visible as a protrusion on the upper terrace. The tip approach to a single Pb adatom exhibited an abrupt change of the conductance at the tunneling-to-contact transition and a linear variation of the conductance in the contact range. A hysteresis loop of the conductance was observed for the adatom, too, albeit considerably less pronounced than on clean Pb(111). A representative example is shown in Fig. 3.1(b) in which the conductance hysteresis appears with a width of  $\approx 50$  pm. Imaging the adatom after conductance data acquisition showed that no material had been transferred to the surface.

While the conductance traces in Figs. 3.1(a), (b) represent specific data sets Figs. 3.1(c), (d) comprise all conductance data as density plots. These density plots illustrate the propensity of single-adatom contacts to exhibit smaller conductance hysteresis widths than junctions on clean Pb(111) surfaces. For

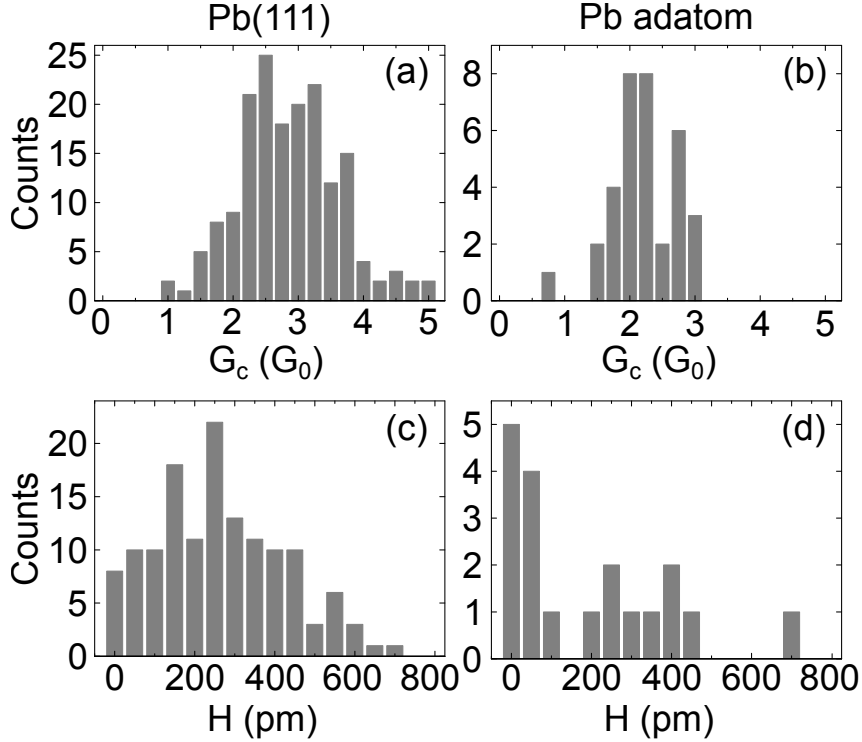


Figure 3.2: Histograms of observed contact conductances ( $G_c$ ) on pristine Pb(111) (a) and on single Pb adatoms (b). (c), (d) Histograms of hysteresis widths ( $H$ ) observed from closing and subsequent opening of junctions comprising Pb(111) (c) and single Pb adatoms (d). All contacts were formed with bias voltages in the range  $10 \text{ mV} \leq |V| \leq 50 \text{ mV}$ . This figure was reproduced from [48] with permission from the American Physical Society.

clarity the data sets of Figs. 3.1(a), (b) were added to the density plots as black lines.

Statistics were performed for the contact conductance,  $G_c$ , and the hysteresis width,  $H$ , in order to more thoroughly compare contact experiments on clean Pb(111) and on single Pb adatoms on Pb(111). To this end  $G_c$  was defined as the conductance value that is reached directly after the jump to contact. The hysteresis width was defined as follows [Fig. 3.1(a)]. A horizontal line starting from  $G_j$  – the conductance just before the jump to contact – intersects the conductance trace acquired during retraction. The difference of the corresponding displacements is referred to as  $H$ .

Figures 3.2(a), (b) show histograms of  $G_c$  obtained for contacts comprising Pb-covered W tips and the clean Pb(111) surface [Fig. 3.2(a)] and single Pb



adatoms on Pb(111) [Fig. 3.2(b)]. The distribution of  $G_c$  for contacts on Pb(111) exhibited a broad maximum at  $\approx 2.5 G_0$ . Contacts on three-layer thick Pb films on Ag(111) were previously reported to exhibit similar conductances. [32] However, these contact conductances were observed less frequently than contact conductances of  $\approx 1.4 G_0$ . [32] Junctions comprising a single Pb adatom showed a maximum in the histogram of  $G_c$  that is more sharply peaked between  $2 G_0$  and  $2.25 G_0$ . The different widths of the conductance histograms are assigned to the degree of precise knowledge of the contact geometry. The Pb(111) surface was not imaged with atomic resolution. Therefore, whether contact was formed to on-top, hollow or bridge lattice sites of Pb(111) remained elusive. In contrast, contact to the adatom left less doubt to the junction geometry at the substrate and thus led to a sharper distribution of  $G_c$ . These findings are in agreement with results obtained for Ag(111), Cu(111) [41] and Au(111). [42, 43] Below we will show that contact conductances calculated for different lattice sites and tip geometries corroborate the experimental results (Table 3.1).

Histograms of the hysteresis widths are different for Pb(111) [Fig. 3.2(c)] and Pb adatoms [Fig. 3.2(d)], too. For contacts on clean Pb(111) the distribution is broad with a maximum at  $\approx 250$  pm. Junctions comprising Pb adatoms most frequently exhibit conductance hysteresis widths between 0 pm and 50 pm. In the probed bias voltage range  $10 \text{ mV} \leq |V| \leq 50 \text{ mV}$  and within the uncertainty margins the hysteresis width did not depend on the sample voltage [Fig. 3.3]. Moreover, the potential influence of Pb phonons was not explored since bulk and surface phonon energies are below 10 meV. [56]

For both contact types breaking of the junctions was accompanied by conductance instabilities before the jump out of contact occurred. These findings are different from results reported for Au contacts. [25] The hysteretic conductance variations in Au contacts were characterized by clear jumps to contact and jumps out of contact. Stretching of the Au junctions led to a gradual decrease of the conductance without the occurrence of conductance fluctuations. These observations were rationalized in terms of junctions in which no further atomic reorganizations took place, *i. e.*, the closing and opening of the Au contacts was understood by elastic deformations of the electrodes. [25] For Pb, however, our *ab initio* quantum mechanical calculations showed that reorganizations of the electrode structure occurred, *i. e.*, the junctions were characterized by

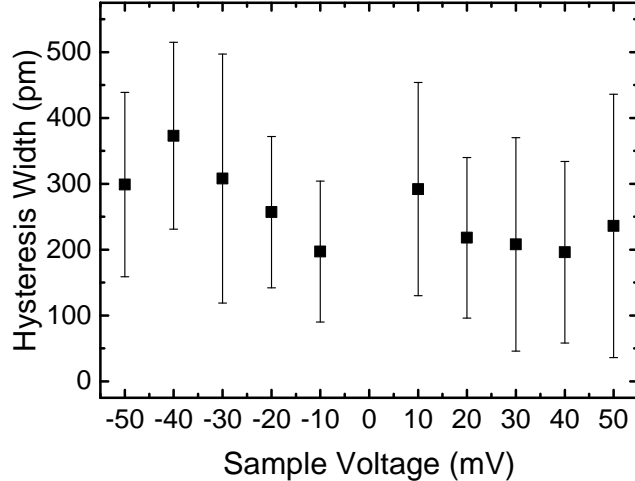


Figure 3.3: Hysteresis width  $H$  of Pb contacts as a function of the sample voltage. The uncertainty margins reflect standard deviations of the different data sets.

plastic deformations. In particular, several atoms were involved in forming and breaking of the contact. This interpretation is compatible with our observation that the hysteresis width slightly increased with increasing contact conductance [Fig. 3.4].

In order to rationalize the experimental data and gain insight into the relation between the mechanical or structural properties and the conductance of the contacts, a full set of density functional calculations was performed. While it is common practice to address the mechanical behavior of contacts at the nanometer scale through molecular dynamics and effective interatomic potentials, [57] the detailed and controlled nature of the present experiments called for taking quantum effects on the forces into account. Both the mechanical behavior and the electron transport were addressed by means of our code ANT.G [58, 59] in combination with Gaussian. [60] The atomic and electronic structure of the relevant contact region were obtained in a fully self-consistent manner and translated into a conductance through a standard Green function formalism with the help of effective self-energies representing the far and less relevant part of the system. [58, 59, 61, 62] To expand the electronic density and represent the Green function, the CRENBS minimal basis set was typically used, with one  $s$  and three  $p$  orbitals, including its corresponding core pseudo-potentials. [63] Additionally, calculations with larger basis sets such as the

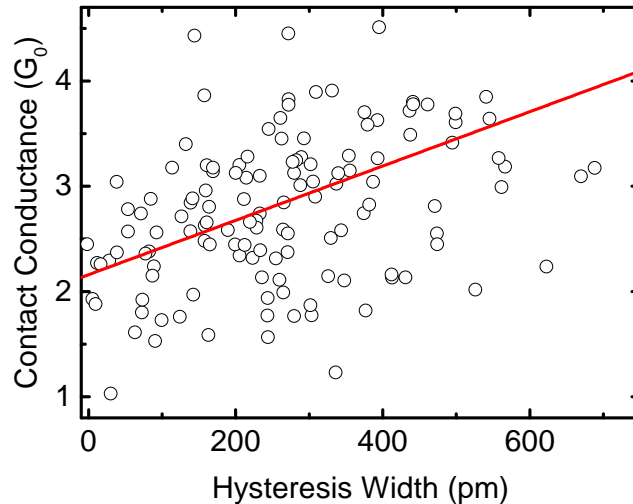


Figure 3.4: Contact conductance  $G_c$  versus hysteresis width  $H$  for all junctions established between the tip and the flat surface investigated in the experiments. The full line represents a linear fit to the data with a slope of  $2.6 \cdot 10^{-3} G_0/\text{pm}$ .

LANL2DZ were performed. [64] However, the resulting atomic and electronic properties were virtually identical to the findings obtained by the minimal basis sets. Tight-binding calculations of the electronic structure for the same geometries led to similar results. A standard local density approximation to the density functional was used. The choice of the functional is not critical to the results for mono-elemental *sp* metals. The specific procedure to mimic the experiments involved successive instantaneous structural relaxations subject to certain geometrical constraints on the boundary atoms of our system which coupled to the bulk substrate and the rest of the tip.

The geometry of the surface and of the contact was known to a very good extent owing to the imaging capabilities of the STM. However, to reduce the large number of possible atomic coordinates the starting atomic structure of the tip prior to contact had in part to be guessed. For all calculations Pb tips grown in the  $\langle 100 \rangle$  and  $\langle 111 \rangle$  direction were chosen. This choice was motivated by the findings of several previous works. Pb tips grown along  $\langle 100 \rangle$  and  $\langle 111 \rangle$  directions exhibit  $\{111\}$  facets, which were shown to exhibit the lowest surface energy. [65] Face-centered cubic metals in general realize  $\langle 100 \rangle$  and  $\langle 111 \rangle$  stacking directions, which was demonstrated for, *e. g.*, Au, [23, 66–68] Pt, [68] and Al [69] electrodes. Consequently, four obvious choices

Table 3.1: Calculated contact conductances ( $G_c$ ) and hysteresis widths ( $H$ ) of atom-sized Pb junctions. Pb tips grown in  $\langle 100 \rangle$  and  $\langle 111 \rangle$  direction with apex terminations of  $n = 1, 4$  and  $n = 1, 3$  atoms, respectively, were considered. On pristine Pb(111)  $G_c$  and  $H$  were calculated for contacts to on-top and hollow sites. For contacts comprising a Pb adatom the adatom resided at a Pb(111) hollow site.

stacking direction	$n$	$G_c$ ( $G_0$ )			$H$ (pm)		
		on-top	hollow	adatom	on-top	hollow	adatom
$\langle 100 \rangle$	1	0.7	0.9	0.9	270	180	40
	4	2.2	4.5	2.2	200	140	260
$\langle 111 \rangle$	1	1.5	2.2	1.2	150	410	110
	3	2.4	2.3	2.4	480	530	480

for the tip termination were available, *i. e.*, the commonly assumed single-atom termination for both orientations and a termination via a four-atom or three-atom plane parallel to the surface for tips grown in the  $\langle 100 \rangle$  and  $\langle 111 \rangle$  direction, respectively. While these choices did not cover all possible configurations, the particular preparation of the tip (*vide supra*) certainly reduced the number of possibilities. The clean Pb(111) surface was represented by an embedded three-layer cluster of up to 100 atoms. The calculations revealed that hexagonal close-packed hollow sites of Pb(111) represent energetically favored adsorption sites for single Pb atoms.

Comparing calculated  $G_c$  for  $\langle 100 \rangle$  and  $\langle 111 \rangle$  tips (Table 3.1) similar values were found. A notable exception is  $G_c = 2.2 G_0$  obtained for single-atom terminated  $\langle 111 \rangle$  tips at Pb(111) hollow sites. This elevated conductance may tentatively be ascribed to the particular junction geometry where the tip continues the stacking of the sample. This situation may maximize the transmission of transport channels. We further found that  $\langle 111 \rangle$  tips exhibited larger hysteresis widths than  $\langle 100 \rangle$  tips. Due to the larger surface-to-volume ratio of  $\langle 111 \rangle$  tips less bonds need to be broken in the course of plastic deformations. Therefore,  $\langle 111 \rangle$  tips may be considered less stiff than  $\langle 100 \rangle$  tips, which favors more pronounced hysteresis effects. Apart from this, Table 3.1 reflects that  $\langle 100 \rangle$  and  $\langle 111 \rangle$  tips exhibit similar trends. Consequently, we will concentrate on the findings obtained for  $\langle 100 \rangle$  tips in the following.

Entire conductance traces were calculated for tips approaching to and retracting from on-top and hollow sites of the pristine Pb(111) surface as well

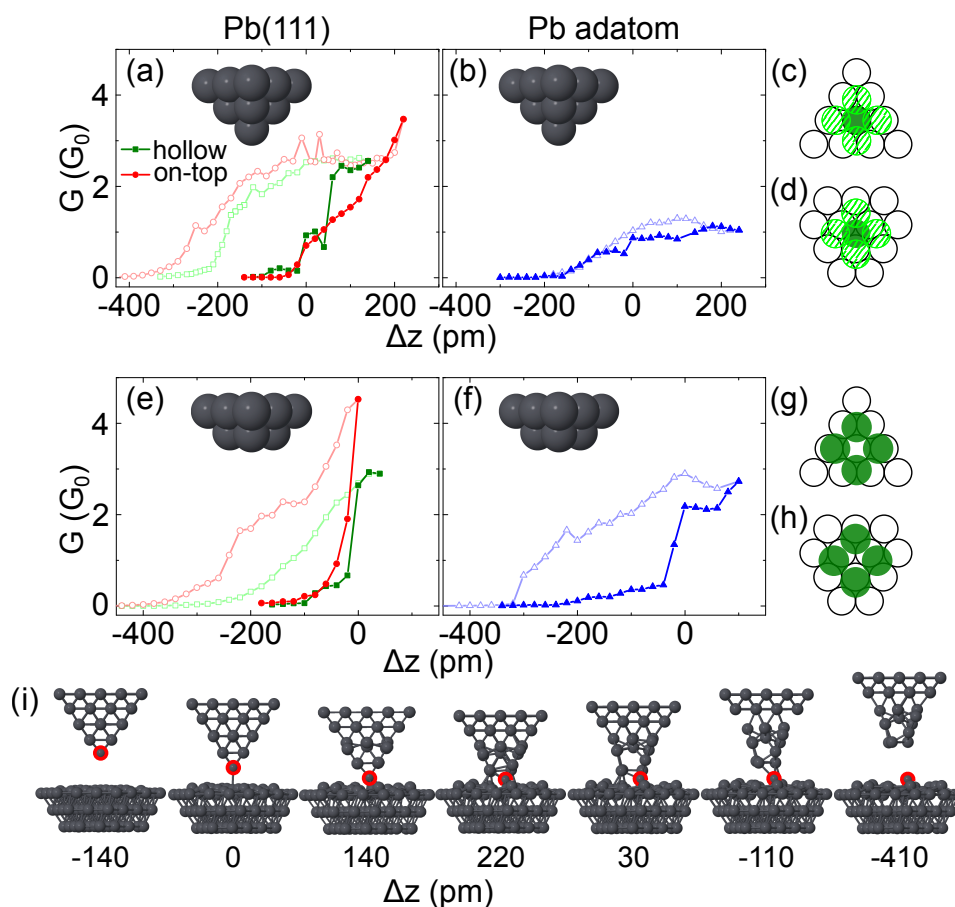


Figure 3.5: Calculated of conductance–distance characteristics for forming and breaking of Pb contacts with a tip grown along the  $\langle 100 \rangle$  direction. (a) A single-atom terminated tip approaches (filled symbols) to and retracts (open symbols) from on-top (squares) and hollow (circles) Pb(111) lattice sites. (b) Same as (a) for a single Pb adatom (triangles). (c), (d) Position of single-atom terminated tip (filled and hatched circles for apex atom and second-layer atoms, respectively) relative to the Pb(111) lattice (circles) for contacts comprising the on-top (c) and the hollow (d) site. (e), (f) Like (a), (b) for a four-atom terminated tip. (g), (h) Position of four-atom terminated tip (filled circles) relative to the Pb(111) lattice (circles) for contacts comprising the on-top (g) and hollow (h) site. (i) Snapshots of calculated contact geometries for a single-atom terminated tip approaching an on-top site of pristine Pb(111). Increasing (decreasing) displacements ( $\Delta z$ ) correspond to tip approach (retraction). Upon retraction the tip apex atom (encircled by a full red line) is transferred to a Pb(111) hollow site adjacent to the approached on-top site. This figure was reproduced from [48] with permission from the American Physical Society.

as Pb adatoms. Representative data obtained for  $\langle 100 \rangle$  tips are shown in Figs. 3.5(a), (e) for Pb(111) and in Figs. 3.5(b), (f) for Pb adatoms. Additionally, conductance traces for single Pb adatoms [Figs. 3.5(b), (f)] were simulated. The orientation of the tip structure with respect to the Pb(111) lattice is indicated for the single-atom [Figs. 3.5(c), (d)] and the four-atom [Figs. 3.5(g), (h)] terminated tip. In the calculations contact formation ( $\Delta z = 0$  pm) was defined by a conductance increase exceeding  $0.3 G_0$  between two subsequent tip displacements. An additional requirement was the variation of the conductance by less than  $0.3 G_0$  for two subsequent displacements in the contact range ( $\Delta z > 0$  pm). According to this definition the single-atom terminated Pb tip exhibited calculated contact conductances of  $G_c = 0.7 G_0$  and  $G_c = 0.9 G_0$  for on-top and hollow sites on Pb(111), respectively [Fig. 3.5(a)]. The geometry of such low-conductance junctions is depicted in Fig. 3.5(i) for the on-top configuration at displacement  $\Delta z = 0$  pm. Distortions of the tip and the substrate were still elastic at this displacement. In particular, the tip apex atom was centered atop the approached Pb(111) atom. The calculations unveiled that the geometry of these low-conductance junctions was unstable. Indeed, the simulations revealed that these junctions exhibited the propensity for atomic relaxations upon further tip approach. Approaching the single-atom terminated tip towards the Pb(111) on-top (hollow) site by 140 pm (60 pm) led to a strong increase of the junction conductance, rather than to a plateaulike variation. The calculated junction geometry showed the implantation of the tip apex atom into the surface [Fig. 3.5(i),  $\Delta z = 220$  pm], which caused the conductance increase.

Forming and breaking of contacts comprising a single-atom terminated tip and the pristine Pb(111) surface revealed hysteretic behavior [Fig. 3.5(a)]. The hysteresis widths were extracted from calculated conductance traces according to the procedure exposed in Fig. 3.1(a). For single-atom terminated tips hysteresis widths of 270 pm and 180 pm were obtained for on-top and hollow sites, respectively (Table 3.1). Figure 3.5(i) further shows that single-atom terminated tips transfer their apex atom to the bare Pb(111) surface upon contact, in agreement with the experimental observation. Upon approaching a Pb(111) on-top site the tip apex atom was transferred to an adjacent hollow site upon contact, reflecting the preferred adsorption site of a single Pb atom.

Junctions comprising an atomically sharp tip and a single Pb adatom showed the conductance–displacement characteristics depicted in Fig. 3.5(b). In contrast to the simulation of contacts comprising the pristine Pb(111) surface a nearly gradual evolution of the conductance in transition range between tunneling and contact was observed, rather than an abrupt jump. The contact conductance was  $\approx 0.9 G_0$  and thus appreciably lower than the averaged experimental value. Only a few number of contacts were experimentally observed with a similarly low conductance [Fig. 3.2(b)]. In addition, a conductance hysteresis was virtually absent for the simulated contacts to adatoms.

The broad range of contact conductances observed in the experiments, *i. e.*,  $\approx 1.0 G_0$  to  $\approx 5.0 G_0$  for Pb(111) and  $\approx 1.5 G_0$  to  $\approx 3 G_0$  for Pb adatoms, could not be explained by tip apices terminated by a single atom alone. According to Table 3.1 calculated contact conductances comprising single-atom terminated  $\langle 100 \rangle$  and  $\langle 111 \rangle$  tips and on-top and hollow sites of Pb(111) range from  $0.7 G_0$  to  $2.2 G_0$ , respectively, while contacts to a single Pb adatom exhibit a conductance range spanning of  $0.9 G_0$  to  $1.2 G_0$ . These deviations to experimental observations represented the impetus to likewise consider junctions comprising tips terminated by more than a single Pb atom in the simulations.

Representative conductance–displacement characteristics are displayed in Fig. 3.5(e) for contacts of  $\langle 100 \rangle$  tips at on-top and hollow Pb(111) sites and in Fig. 3.5(f) for single Pb adatoms residing at Pb(111) hollow sites. In agreement with the experiment abrupt changes of tunneling to contact conductances and jumps out of contact occurred in the calculations. The calculated contact conductance for on-top and hollow Pb(111) sites was  $2.2 G_0$  and  $4.5 G_0$ , respectively. Contacts comprising a four-atom terminated tip and a single Pb adatom exhibited a conductance of  $2.2 G_0$ . Calculations revealed that contacts comprising a four-atom terminated tip apex and on-top sites of Pb(111) involved many atoms in the contact range. In particular, decreasing the tip–surface distance led to an increase of the conductance without reaching a plateaulike conductance variation. Therefore, for this specific junction geometry contact was defined at the same displacement  $\Delta z$  at which contact was reached for junctions comprising four-atom terminated tips and Pb(111) hollow sites.

The calculated hysteresis widths were 200 pm and 140 pm for on-top and hollow sites of Pb(111), respectively, and 260 pm for the Pb adatom. The

simulated hysteresis width for the adatom junction exceeds the experimentally most frequently observed widths between 0 and 50 pm [Fig.3.2(d)]. A few junctions exhibited hysteresis widths in the range of 200 – 450 pm, which are compatible with the calculated result, in particular when  $\langle 111 \rangle$  tips are considered (Table 3.1). For the other ideal contact geometry considered in the calculations, *i. e.*, a single-atom terminated tip and the adatom, an essentially vanishing  $H$  was obtained [Fig.3.5(b)]. Therefore, the experimental junction most likely adopts a geometry within the range of these two extreme and ideal cases. Unlike the simulations based on a single-atom terminated tip, the approach of a four-atom terminated tip to a single Pb adatom on Pb(111) [Fig. 3.5(f)] showed – in accordance with the experiment – an abrupt jump to and out of contact. Therefore, considering both single-atom and four-atom terminated tips in the simulations led to an improved description of the broad conductance distribution observed in the experiments. Furthermore, the conductance hysteresis observed from closing and opening of the junctions was well reproduced.

### 3.4 Conclusion

Closing tunneling junctions comprising Pb tips of an STM and Pb(111) surfaces occurred via an abrupt jump to the first ballistic-conductance plateau. Upon opening such junctions a pronounced hysteretic conductance behavior was observed. In contrast to previously studied Au junctions the Pb conductance hysteresis was not solely due to elastic distortions of the electrodes. Rather, it reflected the plasticity of Pb constrictions even at the ultimate size limit. Additionally, to comprehensively describe electron transport through the biased Pb contacts and mechanical relaxations of the junctions simulations had to deviate from the commonly assumed simple pyramidal tip structure and include more complex tip apices that were terminated by more than a single atom. The presented findings therefore highlight that low-conductance junctions do not necessarily reflect simple junction geometries. Moreover, the results are relevant to mechanical deformations at the nanometer scale.



# 4 Quantum Confinement above Nanocavities at Pb(111)

Reprinted (adapted) with permission from  
Phys. Rev. Lett. **117**, 136803 (2016).  
Copyright 2016 American Physical Society.

We have studied electron states present at the Pb(111) surface above Ar-filled nanocavities created by ion beam irradiation and annealing. Vertical confinement between the parallel crystal and nanocavity surfaces creates a series of quantum well state subbands. Differential conductance data measured by scanning tunneling spectroscopy contain characteristic spectroscopic fine structure within the highest occupied subband, revealing additional quantization. This finding is supported by maps of the differential conductance which show a distinct standing wave pattern. Unexpectedly, reflection at the open boundary where the thin Pb film recovers its bulk thickness gives rise to lateral confinement of electrons.

## 4.1 Introduction

Restricting the motion of electrons in metals or semiconductors to dimensions that are comparable to the Fermi wavelength ( $\lambda_F$ ) is referred to as quantum confinement. The resulting quantized electron states alter the physical properties of the solid, which is beneficial to a variety of applications, *e. g.*, spintronics, [70] quantum computing, [71] optoelectronics, [72, 73] photovoltaics, [74] and catalysis. [75]

An important example for the quantum confinement to one dimension is the occurrence of quantum well states (QWS) in thin films. While quantum well electrons move freely parallel to the thin film their propagation is confined to

the perpendicular direction. The interfaces between vacuum and film as well as film and substrate represent barriers at which the electron waves are reflected. At specific film thicknesses standing electron waves form between the interfaces, the QWS. In the last decades a wealth of experimental and theoretical work on QWS has been reported for a wide variety of film–substrate combinations. [76] The first experimental evidence for QWS was reported from Au films deposited on Ir(111) using the reflection of low-energy electrons. [77] The importance of QWS has been unraveled for, *e. g.*, monitoring film quality, [78] chemical reactivity, [79, 80] crystal growth, [81] magnetic interactions, [82–84] and electron correlation effects such as thin-film superconductivity [85–87] and the Kondo effect. [88, 89]

Lateral electron confinement to two dimensions has likewise been reported. Real-space images of surface electron standing waves in the vicinity of noble-metal step edges belong to the seminal findings in that respect. [90–92] Artificially fabricated atom assemblies acted as quantum corrals for electronic surface states. [93–95] Nanometer-scaled clusters, [96, 97] vacancies [98, 99] as well as molecular networks [100, 101] were shown to effectively confine the electron motion. On narrow terraces [102] and vicinal surfaces [103–105] laterally confined surface states were observed. More recently, electron confinement to graphene nanostructures attracted considerable interest. [106–111]

Further restriction of the electron motion has been demonstrated for atomic [112–116] and molecular [117, 118] chains on surfaces, defects on semiconductor surfaces, [119] colloidal semiconductor nanocrystals, [120] metal [121] and semiconductor [122] quantum dots as well as for artificial atoms. [123] A beautiful demonstration of electron confinement is the observation of the quantum analogue to whispering gallery modes in oligothiophene rings [124] and graphene. [125]

The aforementioned examples clearly reveal the panoply of confinement effects. An important ingredient is common to these examples. In order to restrict the electron motion to a specific region of space a potential well for the reflection of the electron wave is required. The confining potential wells may be provided by geometric constraints, such as boundaries of terraces and quantum corrals, atomic and molecular chain edges, and by the forbidden

electron penetration into the vacuum or surface-projected energy gaps of the substrate.

Here a novel confinement mechanism for conduction electrons of a metal is reported. To this end, nanometer-scaled subsurface voids at Pb(111) were used [Fig. 4.1(a)]. These cavities were fabricated by the impact of  $\text{Ar}^+$  ions and buried several atomic layers underneath the Pb(111) surface. Similar structures were previously reported for Al(111), [45] Cu(100), [46, 126, 127] Cu(110), [126, 128] Ag(100) [129] and Ag(111)[129]. The voids offer the unique opportunity to investigate vertical and lateral confinement. Vertical confinement between Pb(111) and the surface of the cavity leads to the appearance of QWS. In addition, reflection at the open boundaries where the thin Pb film above the nanocavity recovers its bulk thickness leads to lateral confinement, that is, confinement is achieved without confining potential wells. We support our experimental findings using a semi-analytic model accounting for the main features and discuss the role of elastic and inelastic scattering on the confined electron lifetimes. Furthermore real-space images of electron standing wave patterns and the extraction of the relevant Pb band dispersion is presented.

## 4.2 Experiment

Experiments were performed with a scanning tunneling microscope (STM) operated in ultrahigh vacuum ( $10^{-9}$  Pa) and at low temperature (6 K). Atomically clean Pb(111) was obtained by repeated  $\text{Ar}^+$  bombardment and annealing. To efficiently create subsurface voids the ion kinetic energy and current density at the sample were set to 1.1 keV and  $5 \mu\text{Acm}^{-2}$ , respectively, with the ion beam impinging onto the surface at an angle of  $30^\circ$  with respect to the surface normal. Samples were subsequently annealed at 560 K for 20 min. All STM images were recorded at constant current with the bias voltage applied to the sample. Spectra of the differential conductance ( $dI/dV$ ) were acquired by modulating the sample voltage ( $5 \text{ mV}_{\text{pp}}$ , 6.3 kHz) and detecting the current response with a lock-in amplifier.

## 4.3 Results and Discussion

### 4.3.1 Spectroscopic Signatures

STM images of the prepared surface confirm the presence of Ar-filled subsurface cavities [Fig. 4.1(a)] with cross sectional diameters in the 2.5–7 nm range, as previously reported at Al, Cu and Ag surfaces [45, 127–129, 131], and which result from the diffusion and aggregation during annealing of implanted Ar, most likely as Ar+vacancy complexes [126]. Spectra of  $dI/dV$  acquired atop their centers contain considerable structure [Fig. 4.1(b)] attributable to quantum well states (QWS) associated with vertical confinement of electrons between the surfaces of the buried cavity and the crystalline sample. Calculations of QWS energies within thin Pb films show a distinctive thickness dependence. Based upon a comparison with QWS energies found using density functional theory [inset to Fig. 4.1(b)] we have been able to identify the depth of individual nanocavities. The most abundant Pb film thicknesses above the buried void were 4, 6, 8 atomic layers. This observation is ascribed to the vertical confinement of QWS. Their Fermi wavelength approximately corresponds to four times the Pb layer spacing along (111), *i. e.*,  $\lambda_F \approx 4a_{(111)}$ . Consequently, a bilayer periodicity of the density of states (DOS) at the Fermi energy ( $E_F$ ) may be expected. Similar observations were reported for the bilayer oscillation of the superconducting transition temperature in ultrathin Pb films, [85–87] preferred island heights, [132, 133] and the work function. [134]

The QWS dispersion parallel to the surface in thin Pb films is parabolic near the Brillouin zone center  $\bar{\Gamma}$ , but due to hybridization flattens and disperses downward for larger wave vector  $k$ . As an example, Fig. 4.1(c) shows the dispersion of the highest occupied QWS (HOQWS) for a 4-layer Pb(111) film as a blue line. The hybridization effects increase (and consequently the effective mass) for higher QWS energies, leading to states at  $\approx 1$  eV above the Fermi level  $\varepsilon_F$  and higher having a very narrow line shape in  $dI/dV$  spectra. However, occupied states exhibit an identifiable band width [135], and close inspection of  $dI/dV$  spectra recorded atop the center of cavities reveal additional structure within the band width of the HOQWS, in the form of a series of peaks [indicated by horizontal arrows in the right panel of Fig. 4.1(c)] whose location varies with

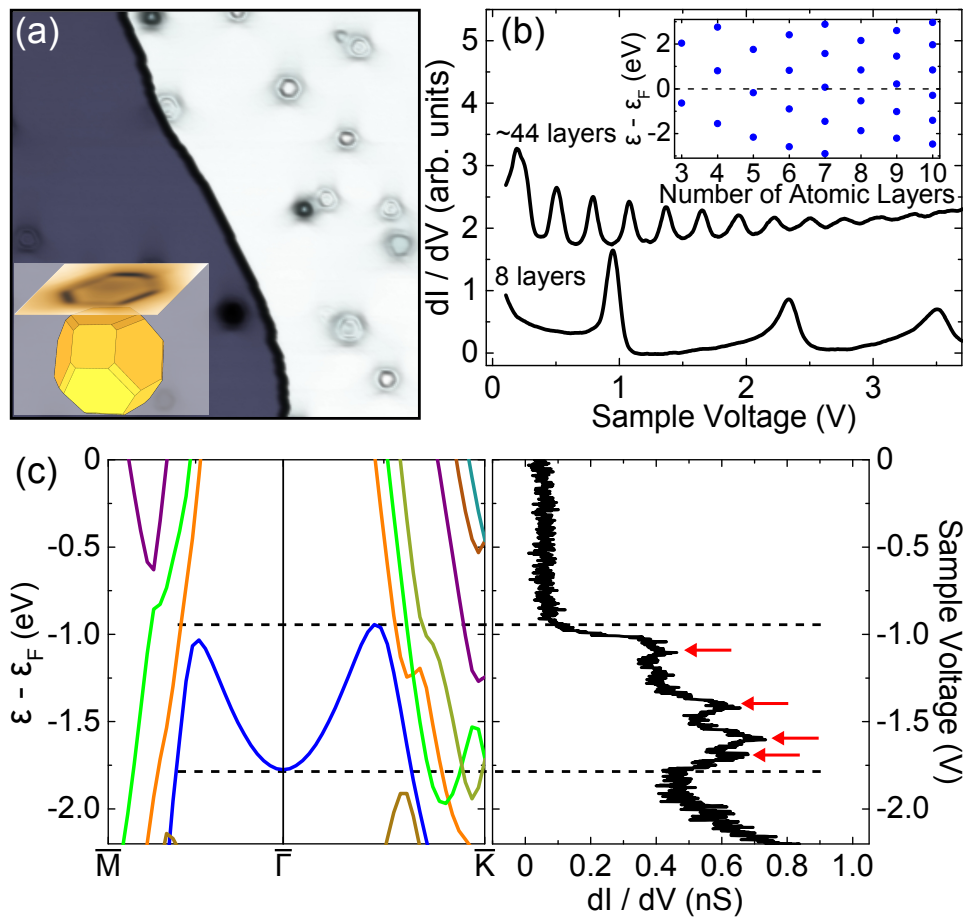


Figure 4.1: (a) STM image of Pb(111) showing buried cavities on a lower (dark gray) and an upper (light gray) terrace (0.5 nA, 1.08 V, 94 nm  $\times$  94 nm). Inset: Schematic illustration of a subsurface nanocavity, with geometry based upon Wulff construction using (111), (110) and (001) Pb surface energies. (b) Constant-current (0.5 nA)  $dI/dV$  spectra (vertically offset) acquired atop cavities located at different depths, exhibiting signatures of unoccupied QWS. Inset: Calculated QWS energies as a function of the Pb layer thickness. (c) Left: Calculated energy band structure of a 4-layer Pb(111) thin film showing the dispersion of the highest occupied QWS (blue line) with a 0.2 eV energy shift applied to align band minimum. Right: Experimental constant-height  $dI/dV$  spectrum acquired atop the center of a subsurface cavity identified as being 4 layers below the surface, showing spectroscopic fine structure (red arrows) within the band of the highest occupied QWS (feedback loop parameters: 1 nA,  $-2.5$  V). This figure was reproduced from [130] with permission from the American Physical Society.

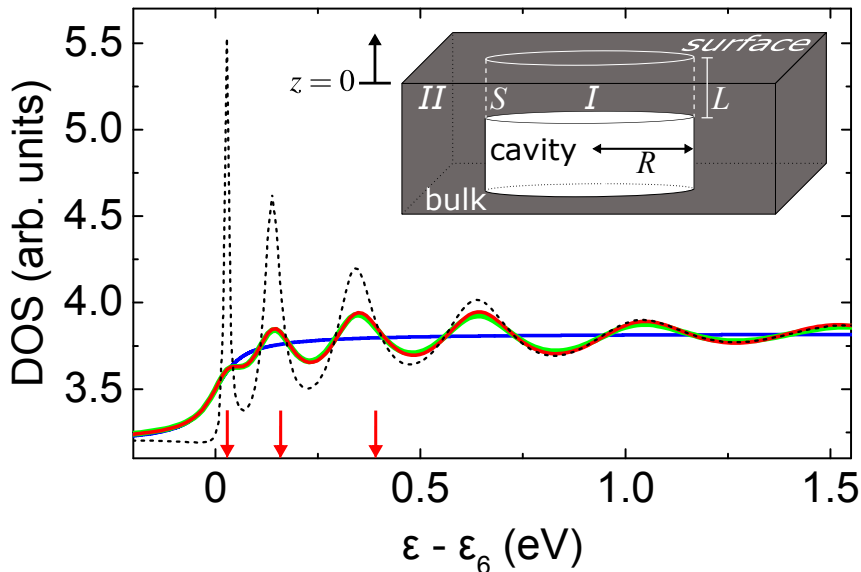


Figure 4.2: Density of states (DOS) of the HOQWS for a 4-layer Pb film (blue) integrated over film thickness, and atop a 2.7 nm radius bubble 4 layers beneath the surface omitting (red) and including (green) interband scattering. The dashed line shows the DOS in the absence of inelastic lifetime broadening ( $\Sigma_i = 0$ ). The arrows in the main figure indicate the expected energies of electrons ideally confined to region  $I$ . Inset: Model geometry and partitioning of space used in calculations. The cavity with radius  $R$  exhibits a surface–vacuum distance  $L$ . Electrons are excluded from the cavity and the vacuum above the surface. Surface  $S$  separates region  $I$ , the space between the cavity and the crystal surface, from region  $II$ , where the electron is no longer confined in the vertical (downwards) direction. This figure was reproduced from [130] with permission from the American Physical Society.

the diameter of the particular subsurface cavity. This structure manifests the existence of additional quantization of the electron states, which we associate with *lateral* confinement to the region between the cavity and the Pb surface.

We base this unusual interpretation of the fine structure in the HOQWS on the model illustrated in the inset to Fig. 4.2, comprising a circularly symmetric cavity of radius  $R$  a depth  $L$  beneath the surface ( $z = 0$ ), with side facets normal to the upper face extending into the bulk ( $z \rightarrow -\infty$ ). Electrons are ideally excluded from the volume of the cavity and the vacuum region outside the crystal, whilst being free to move within the region occupied by Pb; there we set the potential to zero since the relevant Pb states disperse with effective mass  $m^*$  close to the free-electron mass,  $m$ , both normal and parallel to the surface. We find the local density of states (DOS) at energy

$\varepsilon$  as  $\varrho(\mathbf{r}; \varepsilon) = 1/\pi \text{Im } G(\mathbf{r}, \mathbf{r}; \varepsilon)$  where the Green function  $G$  satisfies the inhomogeneous Schrödinger equation  $(\mathcal{H} - \varepsilon)G = \delta(\mathbf{r} - \mathbf{r}')$ . We include in the Hamiltonian  $\mathcal{H} = -\hbar^2/(2m) \nabla^2 + V - i\Sigma_i(\varepsilon)$  a non-Hermitian self-energy term accounting for inelastic lifetime effects, for which we use  $\Sigma_i = \Sigma_{\text{e-ph}} + \Sigma_{\text{e-e}}$  with electron-phonon and electron-electron interaction terms  $\Sigma_{\text{e-ph}} = 12 \text{ meV}$  and  $\Sigma_{\text{e-e}} = \alpha(\varepsilon - \varepsilon_F)^2$ , respectively, with  $\alpha = 0.012 \text{ eV}^{-1}$  from measured values in Pb overlayers [135, 136]. If the cavity has infinite extent ( $R \rightarrow \infty$ ) then integrating over the well width  $L$  the DOS associated with the  $n$ th quantum well subband is  $\varrho_n^\infty(\varepsilon) = m/(2\pi^2\hbar^2) (\pi - \arg(\varepsilon - \varepsilon_n + i\Sigma_i(\varepsilon)))$ , corresponding to a lifetime-broadened steplike increase at the threshold QWS energy  $\varepsilon_n = \hbar^2 n^2 \pi^2 / (2mL^2)$  (blue curve in Fig. 4.2).

For a cavity of finite radius we partition space into regions  $I$  and  $II$ , shown in the inset to Fig. 4.2, separated by surface  $S$ . Working in  $I$  alone, the Green function satisfies the inhomogeneous Schrödinger equation with embedded Hamiltonian [137]  $\mathcal{H}_{\Sigma_S} = \mathcal{H} + \hbar^2/(2m) \delta(\mathbf{r} - \mathbf{r}_S) \mathbf{n}_S \cdot \nabla + \Sigma_S(\varepsilon)$  ( $\mathbf{n}_S$ : surface normal pointing from  $I$  to  $II$ ) where together the second term and surface operator  $\Sigma_S(\varepsilon) = \delta(\mathbf{r} - \mathbf{r}_S) \delta(\mathbf{r}' - \mathbf{r}'_S) \Sigma_S(\mathbf{r}_S, \mathbf{r}'_S; \varepsilon)$  ensure that the Green function in  $I$  matches correctly on  $S$  to the Green function in  $II$ . The embedding potential  $\Sigma_S$  found from  $\mathbf{n}_S \cdot \nabla \psi = -2m/\hbar^2 \int_S \Sigma_S \psi dS'$  for  $\mathbf{r} \in S$ , where  $\psi$  is the solution of the Schrödinger equation in region  $II$  at energy  $\varepsilon$ , is

$$\begin{aligned} \Sigma_S(\mathbf{r}_S, \mathbf{r}'_S; \varepsilon) &= -\frac{\hbar^2}{2m\pi^2 R} \sum_M e^{iM(\phi - \phi')} \int_0^\infty dq \sin(qz) \sin(qz') \times \\ &\quad \left. \frac{d}{dr} \ln[H_M^{(1)}(\sqrt{2m\varepsilon/\hbar^2 - q^2}r)] \right|_{r=R}, \end{aligned} \quad (4.1)$$

with  $H_M^{(1)}$  the Hankel function and  $M$  the angular momentum quantum number. Finally, expanding the Green function in region  $I$  as

$$\begin{aligned} G(\mathbf{r}, \mathbf{r}'; \varepsilon) &= \frac{1}{\pi L} \sum_M e^{iM(\phi - \phi')} \sum_{n, n' > 0} \sin(k_n z) \sin(k_{n'} z') \times \\ &\quad \mathcal{G}_{M, n, n'}(r, r', \varepsilon) \end{aligned} \quad (4.2)$$

with  $k_n = n\pi/L$ , we solve for  $\mathcal{G}$ . Further analytic development is possible upon neglecting interband coupling, *i. e.*, the mixing of states with different

$n, n'$ . The virtual coincidence of numerical results obtained by omitting (red curve in Fig. 4.2) and including (green curve in Fig. 4.2) interband coupling validates this approximation. Within this approximation the DOS from the  $n$ th QWS subband integrated over the well width  $L$  above the center of the cavity ( $r = 0$ , whence only states with  $M = 0$  contribute) is  $\varrho_n(\varepsilon) = \varrho_n^\infty(\varepsilon) + m/(2\pi\hbar^2) \operatorname{Re}(2\mathcal{R}_n(\varepsilon)/(1 - \mathcal{R}_n(\varepsilon)))$ , where

$$\mathcal{R}_n(\varepsilon) = \frac{H_0^{(1)'(\kappa_n r)} - \mathcal{L}_n(\varepsilon)H_0^{(1)}(\kappa_n r)}{\mathcal{L}_n(\varepsilon)H_0^{(2)}(\kappa_n r) - H_0^{(2)'(\kappa_n r)}} \Big|_{r=R}, \quad (4.3)$$

with  $' \equiv d/dr$ ,  $\kappa_n = \sqrt{2m\varepsilon/\hbar^2 - k_n^2}$ , and

$$\mathcal{L}_n(\varepsilon) = \int_0^\infty dq \frac{4k_n^2 \sin^2(qL)}{\pi L (q^2 - k_n^2)^2} \times \frac{d}{dr} \ln[H_0^{(1)}(\sqrt{2m\varepsilon/\hbar^2 - q^2}r)] \Big|_{r=R}. \quad (4.4)$$

This DOS is precisely equivalent to that of a system in which electrons are free to move in two dimensions within a circular domain, with  $\mathcal{R}_n$  an effective reflection coefficient whereby an outgoing radial circular wave  $H_0^{(1)}(\kappa_n r)$  results in the incoming wave  $\mathcal{R}_n(\varepsilon)H_0^{(2)}(\kappa_n r)$  following reflection at boundary radius  $R$ . Here the reflection is not caused by a conventional confining potential, but by the *removal* beyond  $R$  of the confinement in the perpendicular direction, with  $\mathcal{R}_n$  vanishing if the electron remains confined to a depth  $L$  in region *II*. In effect, the electron is reflected by the “open door” that exists beyond the cavity, should it attempt to move deeper into the crystal.

The consequences of this reflection and concomitant confinement are visible in the calculated density of states of the QWS subband, with Fig. 4.2 showing the energy variation using parameters appropriate to the HOQWS of a 4-layer Pb film above a cavity with  $R = 2.7$  nm. There is good correspondence between the features exhibited by the DOS and the structure observed in the measured  $dI/dV$  spectra recorded atop subsurface cavities, Fig. 4.1(c). In particular, the steplike increase characteristic of the thin film ( $R \rightarrow \infty$ ) is replaced by a series of quantized resonant levels, this being especially apparent if the effects of inelastic lifetime broadening processes are suppressed in the calculations



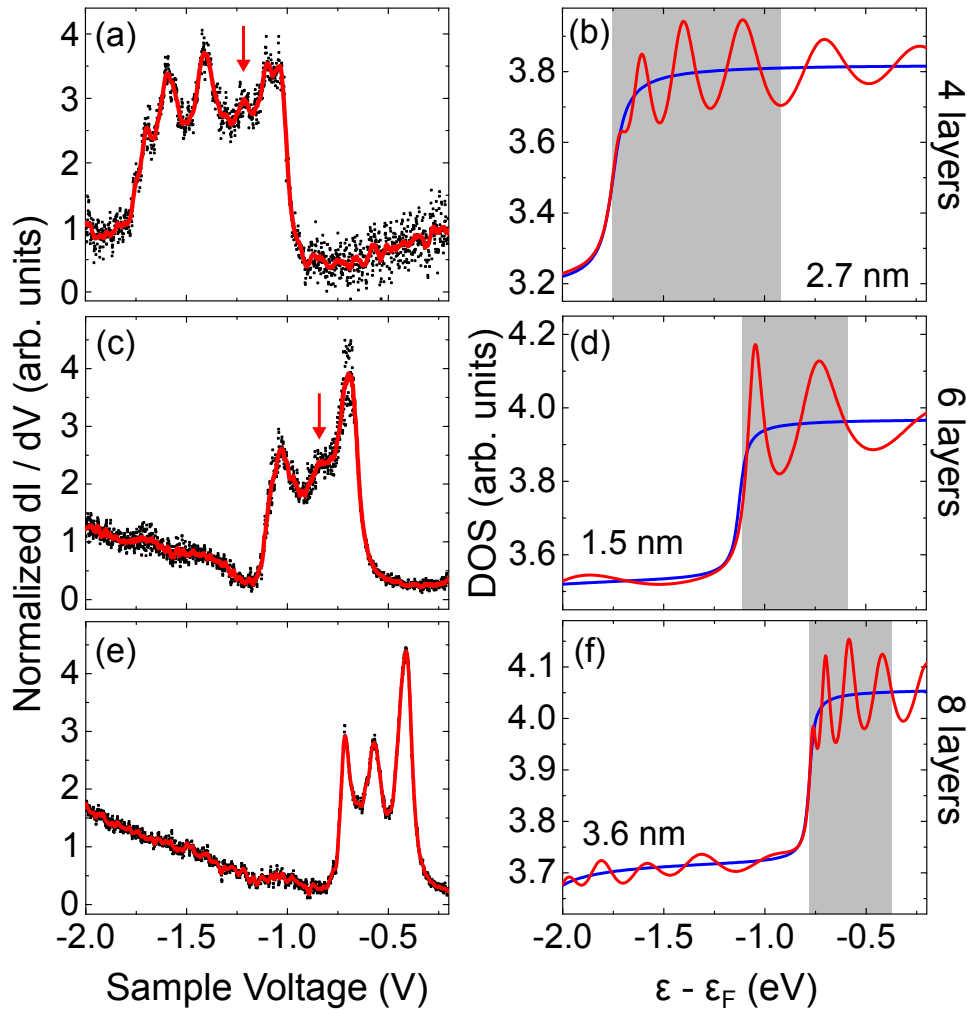


Figure 4.3: (a), (c), (e) Experimental  $dI/dV$  spectra [feedback loop parameters: 1 nA,  $-2.5$  V (a),  $-2$  V (c), (e)]. The data were normalized [12] to ensure an improved approximation to the DOS. Arrows in (a) and (c) indicate additional spectroscopic features caused by the reduced symmetry of the (111) facets. (b), (d), (f) Calculated DOS of the HOQWS atop cavities of indicated radii and depths. Shaded areas in (b), (d), (f) show the range of energies with parabolic HOQWS dispersion. This figure was reproduced from [130] with permission from the American Physical Society.

( $\Sigma_i = 0$ ; dashed line in Fig. 4.2). Further measured and calculated spectra are presented in Fig. 4.3 for different cavity depths and sizes, with the range of energies for which the HOQWS exhibits parabolic dispersion — above this the model is no longer applicable. It is worth noting that we have confirmed using similar methods to those in Ref. [138] that additional low-amplitude peaks present in the experimental  $dI/dV$  spectra (arrows in Fig. 4.3) are consistent with expected contributions from lower symmetry states at slightly off-center locations in domains with  $C_{3v}$  symmetry, appropriate to the (111) faces of the polyhedral cavities given by the Wulff construction.

The resonances in calculated spectra can be identified with poles in the Green function that occur when  $\mathcal{R}_n(\varepsilon) = 1$ , which requires  $d/dr \ln J_0(\kappa_n r)|_{r=R} = \mathcal{L}_n(\varepsilon)$ . Using asymptotic forms, this becomes  $\tan(\kappa_n R - \pi/4) = -\mathcal{L}_n(\varepsilon)/\kappa_n$ . Numerically, we find  $\text{Re } \mathcal{L}_n(\varepsilon) < 0$ , slowly varying and only weakly dependent upon  $R$ . Then with  $\kappa_n \rightarrow 0$  as  $\varepsilon \rightarrow \varepsilon_n$  from above, the lowest energy resonances correspond closely to the positive asymptotes of the tangent, occurring when  $\kappa_n R - \pi/4 \simeq \pi/2, 3\pi/2, \dots$ , or equivalently at energies close to

$$\varepsilon - \varepsilon_n = \frac{\hbar^2(3\pi/4)^2}{2mR^2}, \frac{\hbar^2(7\pi/4)^2}{2mR^2}, \dots \quad (4.5)$$

These are the same energies that would arise for hard-wall reflection at the cavity edge, indicating that the open boundary acts as an effective confining barrier. These values are indicated in Fig. 4.2 as arrows. For higher-order members of the series the increase in  $\kappa_n$  means the actual value of the logarithmic derivative  $\mathcal{L}_n(\varepsilon)$  becomes more important. The resonance energies, therefore, occur increasingly below these values (compare the position of arrows and maxima of red, green and dashed curves in Fig. 4.2).

In contrast to the HOQWS the spectroscopic signature of the lowest unoccupied QWS is much simpler which becomes clear in direct comparison. Figure 4.4(a) shows  $dI/dV$  spectra acquired atop the center of cavities buried 4, 6, 8 atomic layers beneath the Pb(111) surface. All spectra reveal the signature of the highest occupied QWS (HOQWS), which covers a rather broad range of voltages. The broad lineshape of the HOQWS is due to the band structure of thin Pb films that exhibits an increasing effective mass for increasing QWS energy. [139, 140] Concomitantly, the band width decreases giving rise to

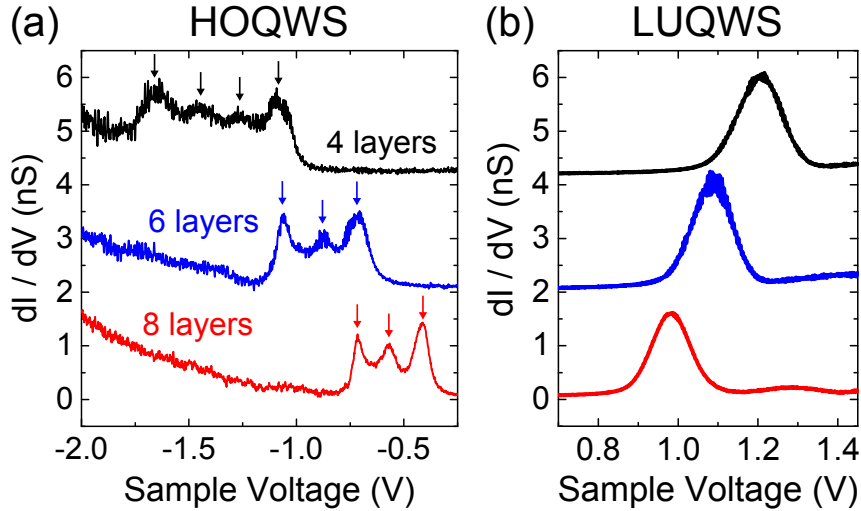


Figure 4.4: (a) Constant-height spectra of  $dI/dV$  acquired atop the center of different cavities with indicated depths showing the highest occupied QWS (HOQWS). The spectra for 6 and 4 layers were vertically offset by 2 nS and 4.1 nS, respectively. The arrows indicate the spectroscopic fine structure due to lateral confinement. Prior to data acquisition the feedback loop had been disabled at 1 nA,  $-2$  V for all spectra. (b) Like (a) for the lowest unoccupied QWS (LUQWS). The spectra for 6 and 4 layers were vertically offset by 2 nS and 4.2 nS, respectively. The feedback loop had been disabled at 0.5 nA, 2.3 V prior to data acquisition.

broad signatures of the HOQWS and narrow, lorentz-like lineshape of the lowest unoccupied QWS (LUQWS), Fig. 4.4(b). [135]

### 4.3.2 Line Widths

The finite resonance widths  $\Gamma$  (full width at half maximum, FWHM) also signal that confinement due to reflection at the open boundary is not ideal, with electrons persisting in the states only for time  $\tau = \hbar/\Gamma$ . We observe that there is a crossover between states at lower energies for which the lifetime is limited by intrinsic inelastic effects (e-ph and e-e scattering) to states at higher energies for which passage through the open boundary and escape into the Pb bulk is limiting. The elastic decay rate for electrons at the center of a circular domain of radius  $R$  is  $\Gamma_e/\hbar \simeq v_g/(2R)(1 - |\mathcal{R}|^2)$  with  $v_g/(2R)$  the boundary collision rate and  $1 - |\mathcal{R}|^2$  the escape probability per attempt. Here the group velocity  $v_g = \sqrt{2(\varepsilon - \varepsilon_n)/m}$  for parabolic dispersion, and  $\mathcal{R}$  is given by Eq. (4.3). Figure 4.5 displays total line widths,  $\Gamma$ , of laterally confined QWS

( $\Gamma = \Gamma_i + \Gamma_e$ ,  $\Gamma_i = \Gamma_{e-ph} + \Gamma_{e-e}$ ) from calculated DOS (squares) and experimental  $dI/dV$  spectra (dots), which are related to decay rates *via*  $1/\tau = \Gamma/\hbar$ .<sup>1</sup> The calculated data show how elastic decay rates become increasingly suppressed as the electron energy approaches, from above, the threshold QWS energy. This is a direct consequence of the decreasing electron velocity impacting upon the collision rate, but also of an increasing reflection probability, as pointed to by the near-linear rather than square-root energy variation in  $\Gamma$ . The inset to Fig. 4.5 shows how  $|\mathcal{R}|$  tends to unity as the increasing lateral de Broglie wavelength of the near-threshold electrons increases sensitivity to the change in the environment at the cavity edge.

Experimentally, the FWHM of the laterally confined QWS electrons was extracted by fitting a superposition of Lorentzians and linear background to  $dI/dV$  data acquired above 6-layer deep cavities with radii between 1.5 nm and 2.2 nm. The measured line widths are broadly consistent with the range of calculated values at lower energies, but peak approximately 0.2–0.25 eV above the HOQWS onset and then decrease. A cluster of values, encircled in Fig. 4.5, that deviate noticeably from the calculated values occur at energies close to the upper edge of the HOQWS band [see Fig. 4.1(c), left panel for the 4-layer case], where  $v_g$  — and thus  $\Gamma$  — decrease in a manner not described by our model.

### 4.3.3 Quantum Well State Dispersion

Figure 4.6 shows the pseudo-three-dimensional STM image of a freshly prepared Pb(111) surface. The inset to Fig. 4.6 presents a constant-current  $dI/dV$  map of the indicated cavity and reveals a rich structure. In the center of the map a regular hexagonal array of protrusions is visible. This array is assigned to the standing-wave pattern that results from the reflection of QWS electrons at the open boundary where the thin Pb film between the cavity and the Pb(111) surface recovers its bulk thickness. The characteristic voltage-dependent changes in the standing-wave pattern will be used to extract the dispersion of the underlying electron bands.

---

<sup>1</sup>Extracted line widths for cavities buried 4 and 8 layers below the surface can be found in the appendix in figure A.1.

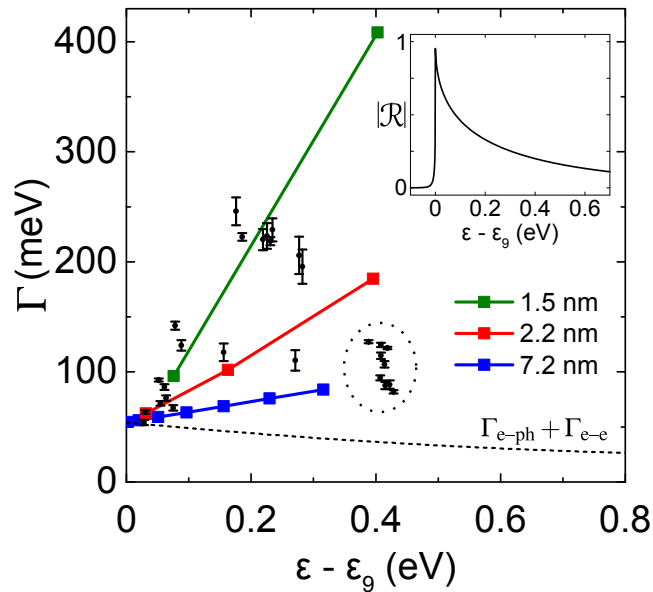


Figure 4.5: Experimentally determined (dots) and calculated (squares) line widths  $\Gamma$  of laterally confined QWS electrons associated with a 6-layer deep cavity as a function of energy. The energy is referenced to the onset energy  $\epsilon_g$  of the HOQWS. Calculations were performed for the indicated cavity radii and represent the sum of inelastic ( $\Gamma_{e-ph} + \Gamma_{e-e}$ , dashed line) and elastic contributions to  $\Gamma$ . Experimental data were obtained for cavity radii ranging between 1.5 nm and 2.2 nm. The data encircled by a dotted line are line widths of confined states with energies close to the flat region of the HOQWS band. Uncertainty margins represent the statistical uncertainty of the fit procedure. Inset: Calculated energy dependence of the reflection coefficient  $|\mathcal{R}|$  at the boundary above a cavity with 2.5 nm radius. This figure was reproduced from [130] with permission from the American Physical Society.

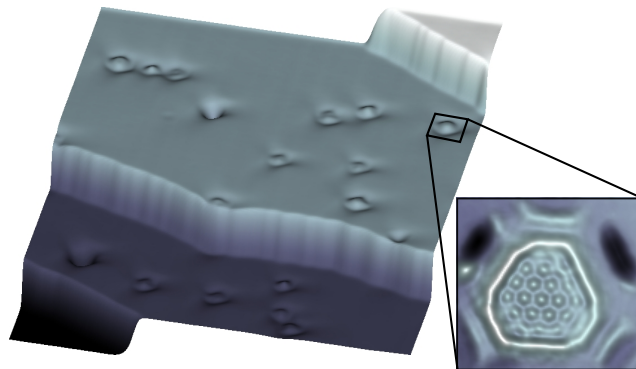


Figure 4.6: Pseudo three-dimensional STM image of Pb(111) showing buried cavities on two terraces (0.5 nA, 1.2 V, 100 nm  $\times$  100 nm). Inset: Constant-current map of  $dI/dV$  recorded atop the indicated cavity showing electron standing wave patterns (1 nA, 0.4 V, 7.8 nm  $\times$  7.8 nm).

Figure 4.7(a) presents a collection of voltage-dependent constant-current  $dI/dV$  maps of a cavity buried 4 atomic layers underneath the Pb(111) surface.<sup>2</sup> The voltage range comprises the HOQWS [ $\approx -1.7$  V, Fig. 4.4(a)] and the LUQWS [ $\approx 1.2$  V, Fig. 4.4(b)]. From  $-1.7$  V to  $-1.1$  V the central interference pattern resembles a set of concentric rings whose number increases with increasing voltage. For voltages  $> -1.0$  V the standing wave pattern changes strongly. Rather than concentric rings a hexagonal arrangement of antinodes appears. With increasing voltage the periodicity of this array increases.

In order to rationalize these observations in terms of an electronic band dispersion mutual distances between nodes and antinodes of electron standing wave patterns [Fig. 4.7(a)] along  $\langle \bar{1}2\bar{1} \rangle$  crystallographic directions [inset to Fig. 4.7(b)] were determined. These distances were identified with  $\lambda/2$  where  $\lambda$  is the electron wavelength. Figure 4.7(b) shows the experimentally extracted dispersion (dots) where  $E - E_F = eV$  ( $e$ : elementary charge) is plotted versus the wave vector  $k = 2\pi/\lambda$ . The full lines in Fig. 4.7(b) present the calculated band structure of a 4-layer thick Pb(111) film along the  $\bar{\Gamma}\bar{M}$  direction of the SBZ. The HOQWS (LUQWS) dispersion appears as a blue (orange) line. The HOQWS exhibits an upper edge at  $\approx 0.5 \text{ \AA}^{-1}$  and  $\approx -1$  eV. This observation explains why maps of  $dI/dV$  at  $\approx -1$  V [Fig. 4.7(a)] do not show clearly resolved interference patterns. Due to the rather flat band in the region around  $\approx 0.5 \text{ \AA}^{-1}$  electron states with various wave vectors and similar energies contribute to the interference pattern, which results in a smeared  $dI/dV$  map. The calculations likewise reveal the rather steep downward dispersion of the LUQWS, which gives rise to the decreasing number of interference antinodes for increasing voltage.

---

<sup>2</sup>The complete gallery with all recorded  $dI/dV$  maps is presented in the appendix in figure A.2. The extracted dispersion relation for 6 and 8 layers can be found in figure A.3.

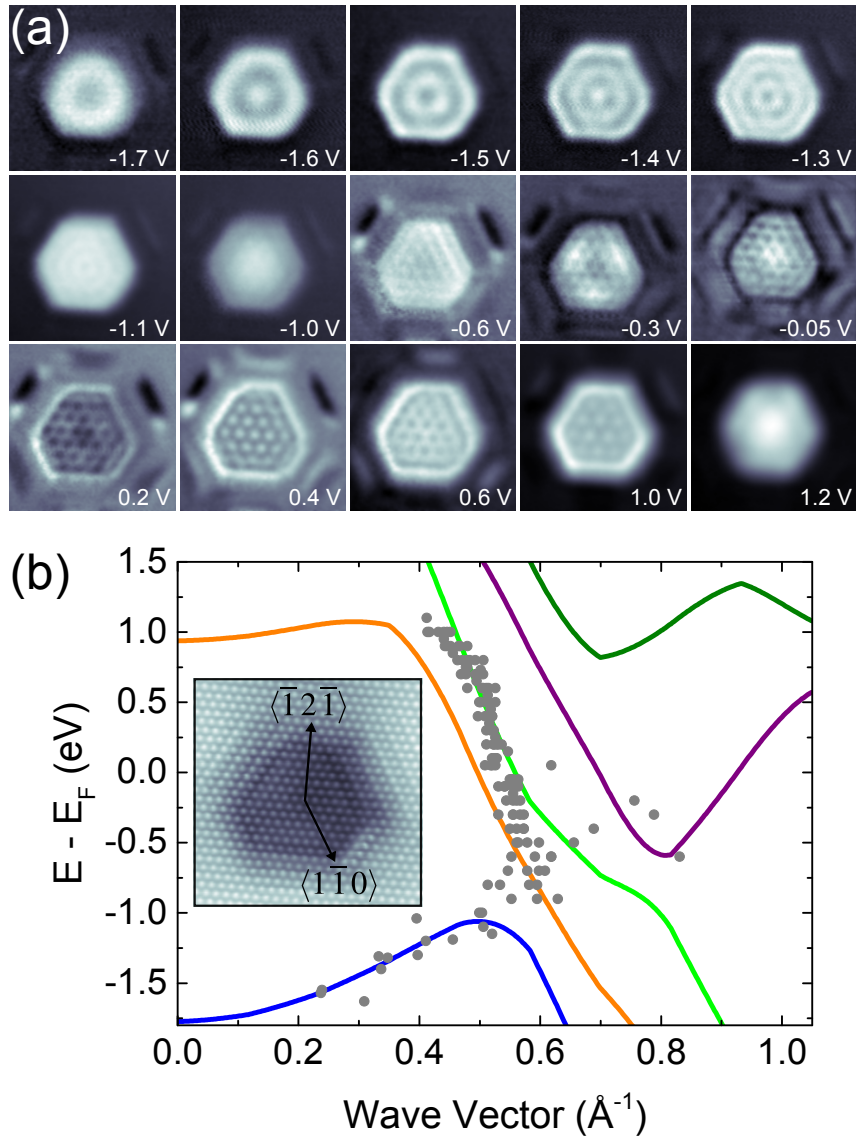


Figure 4.7: (a) Gallery of constant-current  $dI/dV$  maps recorded atop a cavity buried 4 atomic layer underneath the Pb(111) surface at the indicated voltages (1 nA, 7.8 nm  $\times$  7.8 nm). (b) Experimental (dots) and calculated (lines) QWS band dispersion. Experimentally, the wave vector was extracted from the relevant periodicities visible in the  $dI/dV$  maps of six different cavities. The calculations were performed for a 4-layer thick Pb(111) film. The wave vector is oriented along the  $\bar{\Gamma M}$  direction of the SBZ, which corresponds to  $\langle \bar{1}2\bar{1} \rangle$  crystallographic directions. Inset: STM image of the surface region atop a buried cavity with atomic resolution of the Pb(111) lattice and indicated crystallographic directions (0.5 nA, 0.3 V, 7.8 nm  $\times$  7.8 nm).

## 4.4 Conclusion

We have identified through spectroscopic fine structure unexpected additional electronic state quantization atop near-surface cavities at Pb(111). This unprecedented experimental observation is understood to originate from reflection at the open boundary where the thin Pb film recovers its bulk thickness, and which serves to further isolate electrons parallel to the surface. We present a model that accounts for this phenomenon and quantifies aspects of this hitherto unexplored mechanism for electron confinement. Besides potential applications exploiting the cavity size and depth dependence of the confined electron energy levels for future studies of lifetime physics, we expect similar strong electron scattering at open boundaries will occur more generally in systems where electrons exhibit long wavelengths compared to constriction sizes, with beyond Pb other simple metals and semiconductors most likely to provide examples.



## 5 Summary and Outlook

Highly controlled Pb point contacts have been investigated by means of scanning tunneling microscopy. The contacts exhibit a hysteretic behavior upon closing and opening of the contact. Two parameters have been in the focus of the experimental analysis, namely the contact conductance and the hysteresis width. These two parameters contain information about the electronic and mechanical properties of the junction. The hysteretic behavior was reproduced to a high degree by supporting density functional calculations. The presented work revealed that tip shapes deviating from the commonly assumed simple pyramidal configuration are necessary to fully comprehend the experimental results. This conclusion might prove useful for future STM studies in which the tip shape influences the recorded data.

The second part of this thesis dealt with a novel form of quantum confinement in the volume above buried nanocavities. The investigated cavities were buried between 4 and 8 layers below a Pb(111) surface. The electrons in this volume are confined vertically between the crystal surface and the surface of the cavity as well as laterally by the interface at which the thin film and the bulk are separated. A confinement mechanism in this form has not been reported previously. The scanning tunneling microscope allowed the investigation of this effect by its ability to map the local density of states. The lateral confinement causes a fine structure in spectra of the differential conductance as well as a standing wave pattern in maps of the differential conductance. The analysis of line widths provided means to study the elastic decay rates while the standing wave patterns were evaluated to extract the dispersion relation of the QWS subbands. The presented model based on the free electron gas is able to reproduce the majority of experimental observations and captures the basic physics in this system. A follow-up manuscript is currently in progress and is intended to be published in Physical Review B and will contain experimental

data and theoretical descriptions which have not been included in the Physical Review Letters article due to length restrictions. The upcoming manuscript will present the standing wave patterns including the extracted dispersion relation and will show additional recorded spectra of the differential conductance of cavities with varying depths and radii supported by the theoretical model. The presented open boundary scattering is also likely to occur in other systems in which the electron wave lengths are long compared to the size of the constriction. Related effects may be observed in e. g. semiconductor heterostructures and have the possibility to be exploited in applications related to e. g. spintronics, quantum computing, optoelectronics, photovoltaics or catalysis.

# A Quantum Confinement

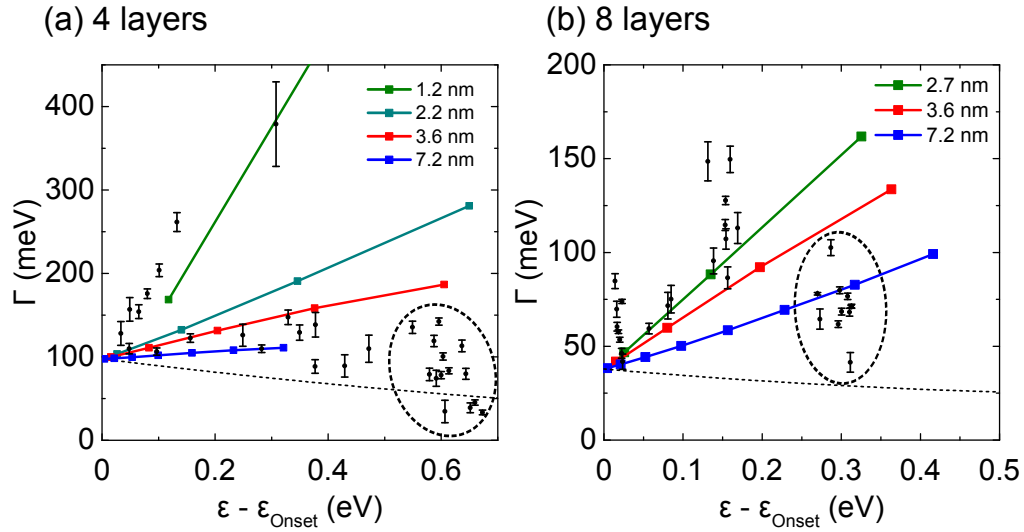


Figure A.1: Experimentally determined (dots) and calculated (squares) line widths  $\Gamma$  of laterally confined QWS electrons associated with 4-layer (a) and 8-layer (b) deep cavities as a function of energy. The energy is referenced to the onset energy of the HOQWS. Calculations were performed for the indicated cavity radii and represent the sum of inelastic ( $\Gamma_{e\text{-ph}} + \Gamma_{e\text{-e}}$ , dashed line) and elastic contributions to  $\Gamma$ . Experimental data were obtained for cavity radii ranging between 1.2 nm and 3.6 nm for (a) and (b). The data encircled by a dotted line are line widths of confined states with energies close to the flat region of the HOQWS band.



Figure A.2: Complete gallery of all  $dI/dV$  maps recorded atop an exemplary cavity buried 4 atomic layer underneath the Pb(111) surface at the indicated voltages (1 nA,  $7.8 \text{ nm} \times 7.8 \text{ nm}$ ). The gallery is an expansion of the  $dI/dV$  maps shown in figure 4.7(a). The majority of the  $dI/dV$  maps show additional elongated structures outside of the central hexagon (red circles at 0.3 V). These modulations of the LDOS have been reported before [128] and can be attributed to electron standing waves between the crystal surface and the edges of the downward sloping Wulff construction which determines the shape of the buried cavity.

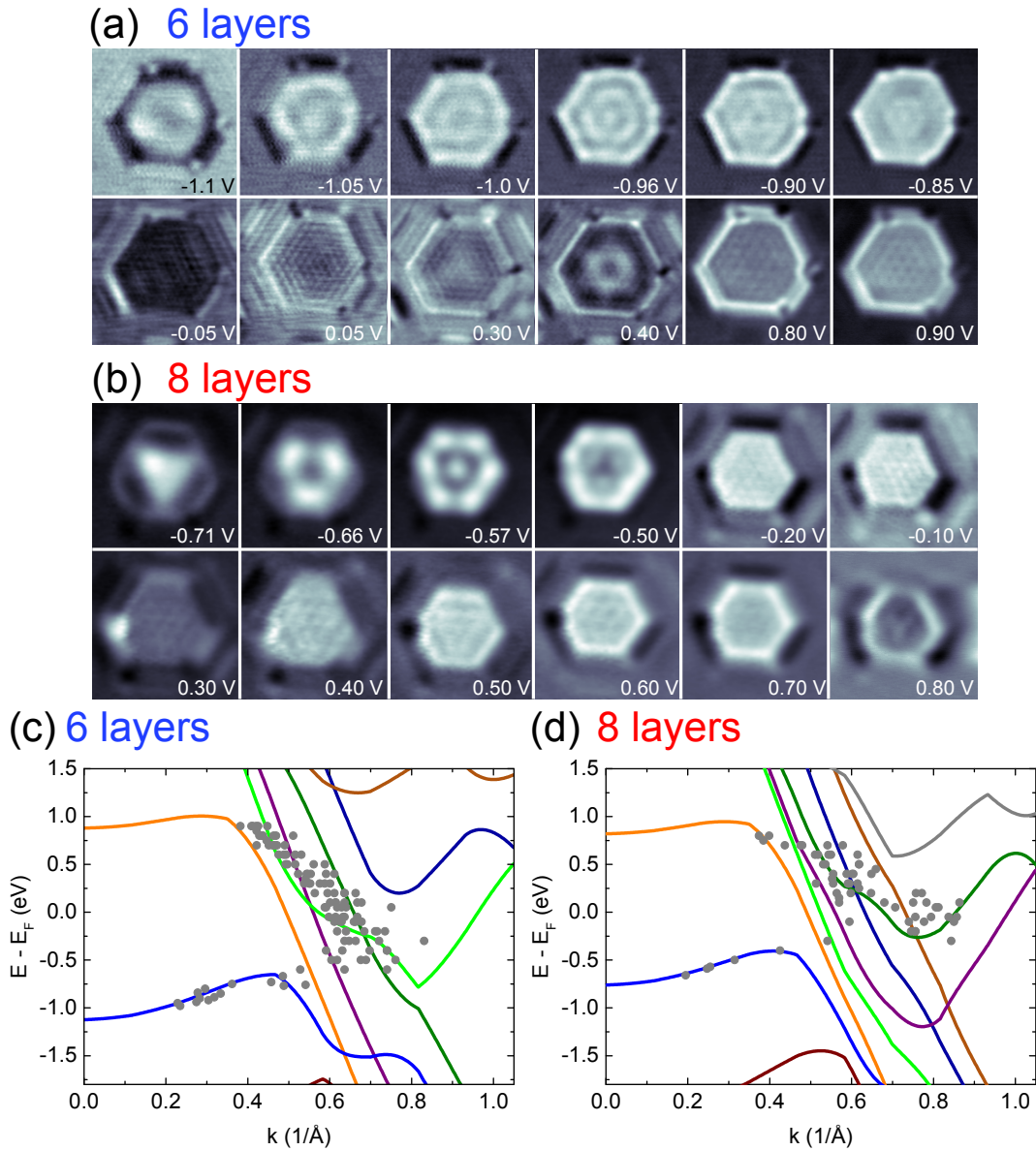


Figure A.3: (a)/(b) Gallery of constant-current  $dI/dV$  maps recorded atop a cavity buried 6 (a) and 8 (b) atomic layer underneath the Pb(111) surface at the indicated voltages (1 nA, (a) 10 nm  $\times$  10 nm, (b) 6.3 nm  $\times$  6.3 nm). (c)/(d) Experimental (dots) and calculated (lines) QWS band dispersion. The calculations were performed for 6-layer (c) and 8-layer (d) thick Pb(111) films. An energy shift of 0.2 eV was applied to align the band minima.



# List of Figures

2.1	Schematic working principle of STM. The tip is brought in vicinity to the sample and a bias $V$ is applied. The resulting tunneling current is amplified and recorded by the STM control unit. The control unit applies the high voltages to the x-, y- and z-piezoes and controls the movement of the tip. During the scan the current is held constant by a feedback loop controlling the z-position of the tip. . . . .	6
2.2	1D square potential barrier with height $V_0$ and width $d$ and schematic wave function $\Psi$ representing the quantum mechanical tunneling process. The wave function inside the barrier decays exponentially and is transmitted with a finite probability. . . . .	7
2.3	Tunneling process in STM for finite bias voltages. Tip and sample are separated by a vacuum energy barrier with a trapezoidal shape determined by the work functions $\Phi_t$ and $\Phi_s$ of tip and sample, respectively. With a positive voltage applied to the sample, the fermi levels $E_F$ of tip and sample shift relatively to each other and electrons tunnel from occupied tip states (light grey) to unoccupied sample states. The DOS of the tip $\rho_t$ is set constant. The arrows indicate the direction of the flowing net current with the length of the arrows symbolizing the relative contributions. With higher energy the transmission probability of the electrons and their impact on the tunneling current increases. . . . .	9

- 
- 2.4 (a) Comparison between a unmodified (black) and a normalized (red) constant-height  $dI/dV$ -spectra showing the HOQWS of a Pb thin-film atop a buried cavity. The normalization was achieved by applying equation (2.15) to the unmodified spectra with the parameters  $\Phi = 4.2$  eV and  $z_0 = 1$  nm. The feedback loop was opened at  $V = -2.5$  V and  $I = 0.5$  nA. (b) Comparison between a  $dI/dV$ -spectra obtained by the numerical differentiation of the  $I(V)$ -curve (blue) and the same unmodified  $dI/dV$ -spectra obtained by Lock-In-technique (black). The feedback loop was opened at  $V = -2$  V and  $I = 0.5$  nA. . . . . 12
- 2.5 Photography of the experimental UHV setup. The most important parts are labeled. The setup consists of two separated chambers, the preparation chamber and the analysis chamber with the mounted cryostat. The load lock chamber allows to load samples into the UHV without breaking the vacuum of the preparation chamber. . . . . 17
- 2.6 Photography of the unmounted STM body. The most important parts are labeled. During measurements the STM body is hanging spring-suspended from the bottom of the liquid helium cryostat. . . . . 19



- 3.1 (a) Representative conductance evolution of a junction comprising Pb(111) and a Pb-coated W tip acquired at 50 mV. Tip approach (black line) leads to an exponential increase of the conductance in the tunneling range (displacements  $\Delta z < 0$  pm). The abrupt change of the conductance from  $G_j = 0.2 G_0$  to  $G_c = 2.9 G_0$  at  $\Delta z = 0$  pm reflects the formation of the contact. In the probed contact range ( $\Delta z > 0$  pm) the conductance increases linearly. Upon tip retraction (gray line) the conductance decreases linearly and reveals instabilities in the form of, *e. g.*, two-level fluctuations (dashed rectangle). The definition of the hysteresis width,  $H$ , is indicated. Inset: Two-level fluctuations observed in the conductance trace upon tip retraction. (b) Like (a) for a contact to a single Pb adatom on Pb(111) with  $G_j = 0.1 G_0$  and  $G_c = 2.2 G_0$ . Inset: Pseudo-three-dimensional representation of an STM image of Pb(111) (0.1 V, 55 pA, 50 nm  $\times$  50 nm). Two terraces are visible. A Pb adatom appears as a protrusion on the upper terrace. Additional structure is due to near-surface voids induced by Ar<sup>+</sup> bombardment. [45, 46] Image processing was performed using WSxM. [47] (c), (d) Density plots of all acquired conductance traces [137 for Pb(111), 19 for single Pb adatoms]. The color scale depicts the number of conductance data linearly grouped into bins defined by a regular 90  $\times$  90 grid, which was spanned from  $-1090$  pm to 260 pm and from  $0 G_0$  to  $7 G_0$ . Full lines are the conductance traces shown in (a), (b). This figure was reproduced from [48] with permission from the American Physical Society. . . . . 26
- 3.2 Histograms of observed contact conductances ( $G_c$ ) on pristine Pb(111) (a) and on single Pb adatoms (b). (c), (d) Histograms of hysteresis widths ( $H$ ) observed from closing and subsequent opening of junctions comprising Pb(111) (c) and single Pb adatoms (d). All contacts were formed with bias voltages in the range  $10 \text{ mV} \leq |V| \leq 50 \text{ mV}$ . This figure was reproduced from [48] with permission from the American Physical Society. 28
- 3.3 Hysteresis width  $H$  of Pb contacts as a function of the sample voltage. The uncertainty margins reflect standard deviations of the different data sets. . . . . 30
- 3.4 Contact conductance  $G_c$  versus hysteresis width  $H$  for all junctions established between the tip and the flat surface investigated in the experiments. The full line represents a linear fit to the data with a slope of  $2.6 \cdot 10^{-3} G_0/\text{pm}$ . . . . . 31

- 3.5 Calculated of conductance–distance characteristics for forming and breaking of Pb contacts with a tip grown along the  $\langle 100 \rangle$  direction. (a) A single-atom terminated tip approaches (filled symbols) to and retracts (open symbols) from on-top (squares) and hollow (circles) Pb(111) lattice sites. (b) Same as (a) for a single Pb adatom (triangles). (c), (d) Position of single-atom terminated tip (filled and hatched circles for apex atom and second-layer atoms, respectively) relative to the Pb(111) lattice (circles) for contacts comprising the on-top (c) and the hollow (d) site. (e), (f) Like (a), (b) for a four-atom terminated tip. (g), (h) Position of four-atom terminated tip (filled circles) relative to the Pb(111) lattice (circles) for contacts comprising the on-top (g) and hollow (h) site. (i) Snapshots of calculated contact geometries for a single-atom terminated tip approaching an on-top site of pristine Pb(111). Increasing (decreasing) displacements ( $\Delta z$ ) correspond to tip approach (retraction). Upon retraction the tip apex atom (encircled by a full red line) is transferred to a Pb(111) hollow site adjacent to the approached on-top site. This figure was reproduced from [48] with permission from the American Physical Society. . . . . 33
- 4.1 (a) STM image of Pb(111) showing buried cavities on a lower (dark gray) and an upper (light gray) terrace (0.5 nA, 1.08 V, 94 nm  $\times$  94 nm). Inset: Schematic illustration of a subsurface nanocavity, with geometry based upon Wulff construction using (111), (110) and (001) Pb surface energies. (b) Constant-current (0.5 nA)  $dI/dV$  spectra (vertically offset) acquired atop cavities located at different depths, exhibiting signatures of unoccupied QWS. Inset: Calculated QWS energies as a function of the Pb layer thickness. (c) Left: Calculated energy band structure of a 4-layer Pb(111) thin film showing the dispersion of the highest occupied QWS (blue line) with a 0.2 eV energy shift applied to align band minimum. Right: Experimental constant-height  $dI/dV$  spectrum acquired atop the center of a subsurface cavity identified as being 4 layers below the surface, showing spectroscopic fine structure (red arrows) within the band of the highest occupied QWS (feedback loop parameters: 1 nA,  $-2.5$  V). This figure was reproduced from [130] with permission from the American Physical Society. . . . . 41

- 4.2 Density of states (DOS) of the HOQWS for a 4-layer Pb film (blue) integrated over film thickness, and atop a 2.7 nm radius bubble 4 layers beneath the surface omitting (red) and including (green) interband scattering. The dashed line shows the DOS in the absence of inelastic lifetime broadening ( $\Sigma_i = 0$ ). The arrows in the main figure indicate the expected energies of electrons ideally confined to region *I*. Inset: Model geometry and partitioning of space used in calculations. The cavity with radius *R* exhibits a surface–vacuum distance *L*. Electrons are excluded from the cavity and the vacuum above the surface. Surface *S* separates region *I*, the space between the cavity and the crystal surface, from region *II*, where the electron is no longer confined in the vertical (downwards) direction. This figure was reproduced from [130] with permission from the American Physical Society. . . . . 42
- 4.3 (a), (c), (e) Experimental  $dI/dV$  spectra [feedback loop parameters: 1 nA,  $-2.5$  V (a),  $-2$  V (c), (e)]. The data were normalized [12] to ensure an improved approximation to the DOS. Arrows in (a) and (c) indicate additional spectroscopic features caused by the reduced symmetry of the (111) facets. (b), (d), (f) Calculated DOS of the HOQWS atop cavities of indicated radii and depths. Shaded areas in (b), (d), (f) show the range of energies with parabolic HOQWS dispersion. This figure was reproduced from [130] with permission from the American Physical Society. 45
- 4.4 (a) Constant-height spectra of  $dI/dV$  acquired atop the center of different cavities with indicated depths showing the highest occupied QWS (HOQWS). The spectra for 6 and 4 layers were vertically offset by 2 nS and 4.1 nS, respectively. The arrows indicate the spectroscopic fine structure due to lateral confinement. Prior to data acquisition the feedback loop had been disabled at 1 nA,  $-2$  V for all spectra. (b) Like (a) for the lowest unoccupied QWS (LUQWS). The spectra for 6 and 4 layers were vertically offset by 2 nS and 4.2 nS, respectively. The feedback loop had been disabled at 0.5 nA, 2.3 V prior to data acquisition. 47

- 4.5 Experimentally determined (dots) and calculated (squares) line widths  $\Gamma$  of laterally confined QWS electrons associated with a 6-layer deep cavity as a function of energy. The energy is referenced to the onset energy  $\varepsilon_9$  of the HOQWS. Calculations were performed for the indicated cavity radii and represent the sum of inelastic ( $\Gamma_{e-ph} + \Gamma_{e-e}$ , dashed line) and elastic contributions to  $\Gamma$ . Experimental data were obtained for cavity radii ranging between 1.5 nm and 2.2 nm. The data encircled by a dotted line are line widths of confined states with energies close to the flat region of the HOQWS band. Uncertainty margins represent the statistical uncertainty of the fit procedure. Inset: Calculated energy dependence of the reflection coefficient  $|\mathcal{R}|$  at the boundary above a cavity with 2.5 nm radius. This figure was reproduced from [130] with permission from the American Physical Society. . . . . 49
- 4.6 Pseudo three-dimensional STM image of Pb(111) showing buried cavities on two terraces (0.5 nA, 1.2 V, 100 nm  $\times$  100 nm). Inset: Constant-current map of  $dI/dV$  recorded atop the indicated cavity showing electron standing wave patterns (1 nA, 0.4 V, 7.8 nm  $\times$  7.8 nm). . . . . 49
- 4.7 (a) Gallery of constant-current  $dI/dV$  maps recorded atop a cavity buried 4 atomic layer underneath the Pb(111) surface at the indicated voltages (1 nA, 7.8 nm  $\times$  7.8 nm). (b) Experimental (dots) and calculated (lines) QWS band dispersion. Experimentally, the wave vector was extracted from the relevant periodicities visible in the  $dI/dV$  maps of six different cavities. The calculations were performed for a 4-layer thick Pb(111) film. The wave vector is oriented along the  $\overline{\Gamma M}$  direction of the SBZ, which corresponds to  $\langle \overline{12\overline{1}} \rangle$  crystallographic directions. Inset: STM image of the surface region atop a buried cavity with atomic resolution of the Pb(111) lattice and indicated crystallographic directions (0.5 nA, 0.3 V, 7.8 nm  $\times$  7.8 nm). . . . . 51

- A.1 Experimentally determined (dots) and calculated (squares) line widths  $\Gamma$  of laterally confined QWS electrons associated with 4-layer (a) and 8-layer (b) deep cavities as a function of energy. The energy is referenced to the onset energy of the HOQWS. Calculations were performed for the indicated cavity radii and represent the sum of inelastic ( $\Gamma_{e-ph} + \Gamma_{e-e}$ , dashed line) and elastic contributions to  $\Gamma$ . Experimental data were obtained for cavity radii ranging between 1.2 nm and 3.6 nm for (a) and (b). The data encircled by a dotted line are line widths of confined states with energies close to the flat region of the HOQWS band. . . . . 55
- A.2 Complete gallery of all  $dI/dV$  maps recorded atop an exemplary cavity buried 4 atomic layer underneath the Pb(111) surface at the indicated voltages (1 nA, 7.8 nm  $\times$  7.8 nm). The gallery is an expansion of the  $dI/dV$  maps shown in figure 4.7(a). The majority of the  $dI/dV$  maps show additional elongated structures outside of the central hexagon (red circles at 0.3 V). These modulations of the LDOS have been reported before [128] and can be attributed to electron standing waves between the crystal surface and the edges of the downward sloping Wulff construction which determines the shape of the buried cavity. . . . . 56
- A.3 (a)/(b) Gallery of constant-current  $dI/dV$  maps recorded atop a cavity buried 6 (a) and 8 (b) atomic layer underneath the Pb(111) surface at the indicated voltages (1 nA, (a) 10 nm  $\times$  10 nm, (b) 6.3 nm  $\times$  6.3 nm). (c)/(d) Experimental (dots) and calculated (lines) QWS band dispersion. The calculations were performed for 6-layer (c) and 8-layer (d) thick Pb(111) films. An energy shift of 0.2 eV was applied to align the band minima. . . . . 57



## Bibliography

- [1] G. Binnig, H. Rohrer, C. Gerber, and E. Weibel, *Appl. Phys. Lett.* **40**, 178 (1982).
- [2] G. Binnig, H. Rohrer, C. Gerber, and E. Weibel, *Phys. Rev. Lett.* **49**, 57 (1982).
- [3] J. Tersoff and D. R. Hamann, *Phys. Rev. Lett.* **50**, 1998 (1983).
- [4] J. Tersoff and D. R. Hamann, *Phys. Rev. B* **31**, 805 (1985).
- [5] J. Bardeen, *Phys. Rev. Lett.* **6**, 57 (1961).
- [6] D. A. Bonnell, *Scanning probe microscopy and spectroscopy: Theory, techniques, and applications*, 2nd ed. (Wiley-VCH, New York, 2001).
- [7] C. J. Chen, *Introduction to scanning tunneling microscopy*, 2nd ed., Monographs on the physics and chemistry of materials, Vol. 64 (Oxford University Press, New York, 2008).
- [8] R. Wiesendanger, *Scanning Probe Microscopy and Spectroscopy* (Cambridge University Press, Cambridge, 1994).
- [9] J. G. Simmons, *J. Appl. Phys.* **34**, 1793 (1963).
- [10] J. G. Simmons, *J. Appl. Phys.* **34**, 2581 (1963).
- [11] A. Castellanos-Gomez, G. Rubio-Bollinger, M. Garnica, S. Barja, Vazquez de Parga, Amadeo L, R. Miranda, and N. Agrait, *Ultramicroscopy* **122**, 1 (2012).
- [12] M. Ziegler, N. Néel, A. Sperl, J. Kröger, and R. Berndt, *Phys. Rev. B* **80**, 125402 (2009).

- 
- [13] M. Meade, *Lock-in Amplifiers: Principles and Applications*, IEE electrical measurement series (P. Peregrinus, 1983).
- [14] Stanford Research Systems, “MODEL SR830 DSP Lock-In-Amplifier,” (2016).
- [15] N. Agraït, A. L. Yeyati, and J. M. van Ruitenbeek, *Phys. Rep.* **377**, 81 (2003).
- [16] J. Kröger, N. Néel, and L. Limot, *J. Phys.: Condens. Matter* **20**, 223001 (2008).
- [17] R. Berndt, J. Kröger, N. Néel, and G. Schull, *Phys. Chem. Chem. Phys.* **12**, 1022 (2010).
- [18] S. Sanvito, *Chem. Soc. Rev.* **40**, 3336 (2011).
- [19] G. E. W. Bauer, E. Saitph, and B. J. van Wees, *Nat. Mater.* **11**, 391 (2012).
- [20] Y. Dubi and M. Di Ventra, *Rev. Mod. Phys.* **83**, 131 (2011).
- [21] Y. F. Wang, J. Kröger, R. Berndt, H. Vázquez, M. Brandbyge, and M. Paulsson, *Phys. Rev. Lett.* **104**, 176802 (2010).
- [22] G. Schull, T. Frederiksen, A. Arnau, D. Sánchez-Portal, and R. Berndt, *Nat. Nanotechnol.* **6**, 23 (2011).
- [23] H. Ohnishi, Y. Kondo, and K. Takayanagi, *Nature* **395**, 780 (1998).
- [24] A. I. Yanson, G. R. Bollinger, H. E. van den Brom, N. Agraït, and J. M. van Ruitenbeek, *Nature* **395**, 783 (1998).
- [25] M. Trouwborst, E. Huisman, F. Bakker, S. van der Molen, and B. van Wees, *Phys. Rev. Lett.* **100**, 175502 (2008).
- [26] N. Agraït, J. G. Rodrigo, G. Rubio, C. Sirvent, and S. Vieira, *Thin Solid Films* **253**, 199 (1994).
- [27] H. E. den Brom, A. I. Yanson, and J. M. van Ruitenbeek, *Physica B* **252**, 69 (1998).



- 
- [28] A. Halbritter, S. Csonka, O. Y. Kolesnychenko, G. Mihály, O. I. Shklyarevskii, and H. van Kempen, *Phys. Rev. B* **65**, 045413 (2002).
- [29] J. G. Rodrigo, H. Suderow, S. Vieira, E. Bascones, and F. Guinea, *J. Phys.: Condens. Matter* **16**, R1151 (2004).
- [30] L. Kuipers and J. W. M. Frenken, *Phys. Rev. Lett.* **70**, 3907 (1993).
- [31] E. Scheer, N. Agraït, J. C. Cuevas, A. L. Yeyati, B. Ludoph, A. Martín-Rodero, G. R. Bollinger, J. M. van Ruitenbeek, and C. Urbina, *Nature* **394**, 154 (1998).
- [32] M. Becker and R. Berndt, *New J Phys* **12**, 113010 (2010).
- [33] H. Kim and Y. Hasegawa, *Phys. Rev. Lett.* **114**, 206801 (2015).
- [34] F.-Q. Xie, F. Hüser, F. Pauly, C. Obermair, G. Schön, and T. Schimmel, *Phys. Rev. B* **82**, 075417 (2010).
- [35] J. G. Rodrigo, V. Crespo, H. Suderow, S. Vieira, and F. Guinea, *Phys. Rev. Lett.* **109**, 237003 (2012).
- [36] C. Brand, H. Pfnür, G. Landolt, S. Muff, J. H. Dil, T. Das, and C. Tegenkamp, *Nat. Commun.* **6**, 8118 (2015).
- [37] K. J. Franke, G. Schulze, and J. I. Pascual, *Science* **332**, 940 (2011).
- [38] M. Ruby, F. Pientka, Y. Peng, F. von Oppen, B. W. Heinrich, and K. J. Franke, *Phys. Rev. Lett.* **115**, 087001 (2015).
- [39] J. C. Cuevas, A. L. Yeyati, A. Martín-Rodero, G. R. Bollinger, C. Untiedt, and N. Agraït, *Phys. Rev. Lett.* **81**, 2990 (1998).
- [40] M. Ruby, B. W. Heinrich, J. I. Pascual, and K. J. Franke, *Phys. Rev. Lett.* **114**, 157001 (2015).
- [41] L. Limot, J. Kröger, R. Berndt, A. Garcia-Lekue, and W. A. Hofer, *Phys. Rev. Lett.* **94**, 126102 (2005).
- [42] J. Kröger, H. Jensen, and R. Berndt, *New J. Phys.* **9**, 153 (2007).

- 
- [43] J. Kröger, N. Néel, A. Sperl, Y. Wang, and R. Berndt, *New J. Phys.* **11**, 125006 (2009).
- [44] K. Jacobi, *Phys. Rev. B* **38**, 5869 (1988).
- [45] M. Schmid, W. Hebenstreit, P. Varga, and S. Crampin, *Phys. Rev. Lett.* **76**, 2298 (1996).
- [46] O. Kurnosikov, O. A. O. Adam, H. J. M. Swagten, W. J. M. de Jonge, and B. Koopmans, *Phys. Rev. B* **77**, 125429 (2008).
- [47] I. Horcas, R. Fernández, J. M. Gómez-Rodríguez, J. Colchero, J. Gómez-Herrero, and A. M. Baro, *Rev. Sci. Instrum.* **78**, 13705 (2007).
- [48] M. Müller, C. Salgado, N. Néel, J. J. Palacios, and J. Kröger, *Phys. Rev. B* **93**, 235402 (2016).
- [49] H. E. van den Brom, A. I. Yanson, and J. M. van Ruitenbeek, *Phys. B Condens. Matter* **252**, 69 (1998).
- [50] A. Sperl, J. Kröger, and R. Berndt, *Phys. Rev. B* **81**, 035406 (2010).
- [51] N. Néel, J. Kröger, and R. Berndt, *Nano Lett.* **11**, 3593 (2011).
- [52] W. Lee, K. Kim, W. Jeong, L. A. Zotti, F. Pauly, J. C. Cuevas, and P. Reddy, *Nature* **498**, 209 (2013).
- [53] F. Flores, P. M. Echenique, and R. H. Ritchie, *Phys. Rev. B* **34**, 2899 (1986).
- [54] S.-C. Li, Y. Han, J.-F. Jia, Q.-K. Xue, and F. Liu, *Phys. Rev. B* **74**, 195428 (2006).
- [55] K. Arenhold, S. Surnev, H. P. Bonzel, and P. Wynblatt, *Surf. Sci.* **424**, 271 (1999).
- [56] I. Y. Sklyadneva, R. Heid, K.-P. Bohnen, P. M. Echenique, and E. V. Chulkov, *J. Phys.: Condens. Matter* **24**, 104004 (2012).
- [57] C. Sabater, C. Untiedt, J. J. Palacios, and M. J. Caturla, *Phys. Rev. Lett.* **108**, 205502 (2012).

- [58] J. J. Palacios, A. J. Pérez-Jiménez, E. Louis, E. SanFabián, and J. A. Vergés, *Phys. Rev. B* **66**, 035322 (2002).
- [59] E. Louis, J. A. Vergés, J. J. Palacios, A. J. Pérez-Jiménez, and E. SanFabián, *Phys. Rev. B* **67**, 155321 (2003).
- [60] M. J. Frisch, G. W. Trucks, H. B. Schlegel, G. E. Scuseria, M. A. Robb, J. R. Cheeseman, G. Scalmani, V. Barone, B. Mennucci, G. A. Petersson, H. Nakatsuji, M. Caricato, X. Li, H. P. Hratchian, A. F. Izmaylov, J. Bloino, G. Zheng, J. L. Sonnenberg, M. Hada, M. Ehara, K. Toyota, R. Fukuda, J. Hasegawa, M. Ishida, T. Nakajima, Y. Honda, O. Kitao, H. Nakai, T. Vreven, J. A. Montgomery, Jr., J. E. Peralta, F. Ogliaro, M. Bearpark, J. J. Heyd, E. Brothers, K. N. Kudin, V. N. Staroverov, R. Kobayashi, J. Normand, K. Raghavachari, A. Rendell, J. C. Burant, S. S. Iyengar, J. Tomasi, M. Cossi, N. Rega, J. M. Millam, M. Klene, J. E. Knox, J. B. Cross, V. Bakken, C. Adamo, J. Jaramillo, R. Gomperts, R. E. Stratmann, O. Yazyev, A. J. Austin, R. Cammi, C. Pomelli, J. W. Ochterski, R. L. Martin, K. Morokuma, V. G. Zakrzewski, G. A. Voth, P. Salvador, J. J. Dannenberg, S. Dapprich, A. D. Daniels, Ö. Farkas, J. B. Foresman, J. V. Ortiz, J. Cioslowski, and D. J. Fox, Gaussian Inc. Wallingford CT (2009).
- [61] J. J. Palacios, A. J. Pérez-Jiménez, E. Louis, and J. A. Vergés, *Phys. Rev. B* **64**, 115411 (2001).
- [62] D. Jacob and J. J. Palacios, *J. Chem. Phys.* **134**, 044118 (2011).
- [63] R. B. Ross, J. M. Powers, T. Atashroo, W. C. Ermler, L. A. LaJohn, and P. A. Christiansen, *J. Chem. Phys.* **93**, 6654 (1990).
- [64] W. R. Wadt and P. J. Hay, *J. Chem. Phys.* **82**, 284 (1985).
- [65] J.-M. Zhang, F. Ma, and K.-W. Xu, *Appl. Surf. Sci.* **229**, 34 (2004).
- [66] V. Rodrigues, T. Fuhrer, and D. Ugarte, *Phys. Rev. Lett.* **85**, 4124 (2000).

- [67] L. G. C. Rego, A. R. Rocha, V. Rodrigues, and D. Ugarte, *Phys. Rev. B* **67**, 045412 (2003).
- [68] C. Evangeli, M. Matt, L. Rincón-García, F. Pauly, P. Nielaba, G. Rubio-Bollinger, J. C. Cuevas, and N. Agraït, *Nano Lett.* **15**, 1006 (2015).
- [69] C. Schirm, M. Matt, F. Pauly, J. C. Cuevas, P. Nielaba, and E. Scheer, *Nat. Nanotechnol.* **8**, 645 (2013).
- [70] S. A. Wolf, D. D. Awschalom, R. A. Buhrman, J. M. Daughton, S. von Molnár, M. L. Roukes, A. Y. Chtchelkanova, and D. M. Treger, *Science* **294**, 1488 (2001).
- [71] G. Burkard, H.-A. Engel, and D. Loss, “Spintronics, quantum computing, and quantum communication in quantum dots,” in *Fundamentals of Quantum Information: Quantum Computation, Communication, Decoherence and All That*, edited by D. Heiss (Springer, Berlin, Heidelberg, 2002) pp. 241–265.
- [72] G. Konstantatos, *Colloidal quantum dot optoelectronics and photovoltaics* (Cambridge University Press, Cambridge, 2013).
- [73] S. Nakamura, *Rev. Mod. Phys.* **87**, 1139 (2015).
- [74] P. V. Kamat, *J. Phys. Chem. Lett.* **4**, 908 (2013).
- [75] J. Zhao, M. A. Holmes, and F. E. Osterloh, *ACS Nano* **7**, 4316 (2013).
- [76] M. Milun, P. Pervan, and D. P. Woodruff, *Rep. Prog. Phys.* **65**, 99 (2002).
- [77] R. E. Thomas, *J. Appl. Phys.* **41**, 5330 (1970).
- [78] J. J. Paggel, T. Miller, and T.-C. Chiang, *Science* **283**, 1709 (1999).
- [79] X. Ma, P. Jiang, Y. Qi, J. Jia, Y. Yang, W. Duan, W.-X. Li, X. Bao, S. B. Zhang, and Q.-K. Xue, *Proc. Natl. Acad. Sci. USA* **104**, 9204 (2007).
- [80] L. Aballe, A. Barinov, A. Locatelli, S. Heun, and M. Kiskinova, *Phys. Rev. Lett.* **93**, 196103 (2004).

- [81] Y. Jia, M. Özer, H. Weiering, and Z. Zhang, “Nanophenomena at surfaces: Fundamentals of exotic condensed matter properties,” (Springer Berlin Heidelberg, Berlin, Heidelberg, 2011) Chap. Quantum Size Effects in the Growth and Properties of Ultrathin Metal Films, Alloys, and Related Low-Dimensional Structures, pp. 67–112.
- [82] J. E. Ortega, F. J. Himpsel, G. J. Mankey, and R. F. Willis, *Phys. Rev. B* **47**, 1540 (1993).
- [83] C. Carbone, E. Vescovo, O. Rader, W. Gudat, and W. Eberhardt, *Phys. Rev. Lett.* **71**, 2805 (1993).
- [84] A. F. Santander-Syro, F. Fortuna, C. Bareille, T. C. Rodel, G. Landolt, N. C. Plumb, J. H. Dil, and M. Radovic, *Nat. Mater.* **13**, 1085 (2014).
- [85] D. Eom, S. Qin, M.-Y. Chou, and C. K. Shih, *Phys. Rev. Lett.* **96**, 027005 (2006).
- [86] Y. Guo, Y.-F. Zhang, X.-Y. Bao, T.-Z. Han, Z. Tang, L.-X. Zhang, W.-G. Zhu, E. G. Wang, Q. Niu, Z. Q. Qiu, J.-F. Jia, Z.-X. Zhao, and Q.-K. Xue, *Science* **306**, 1915 (2004).
- [87] S. Qin, J. Kim, Q. Niu, and C.-K. Shih, *Science* **324**, 1314 (2009).
- [88] A. Zhao, Q. Li, L. Chen, H. Xiang, W. Wang, S. Pan, B. Wang, X. Xiao, J. Yang, J. G. Hou, and Q. Zhu, *Science* **309**, 1542 (2005).
- [89] T. Uchihashi, J. Zhang, J. Kröger, and R. Berndt, *Phys. Rev. B* **78**, 033402 (2008).
- [90] M. F. Crommie, C. P. Lutz, and D. M. Eigler, *Nature* **363**, 524 (1993).
- [91] Y. Hasegawa and Ph. Avouris, *Phys. Rev. Lett.* **71**, 1071 (1993).
- [92] P. Avouris and I.-W. Lyo, *Science* **264**, 942 (1994).
- [93] M. F. Crommie, C. P. Lutz, and D. M. Eigler, *Science* **262**, 218 (1993).
- [94] E. J. Heller, M. F. Crommie, C. P. Lutz, and D. M. Eigler, *Nature* **369**, 464 (1994).

- 
- [95] J. Kliewer, R. Berndt, and S. Crampin, *New J. Phys.* **3**, 22 (2001).
- [96] J. Li, W. D. Schneider, R. Berndt, and S. Crampin, *Phys. Rev. Lett.* **80**, 3332 (1998).
- [97] C. Tournier-Colletta, B. Kierren, Y. Fagot-Revurat, and D. Malterre, *Phys. Rev. Lett.* **104**, 016802 (2010).
- [98] H. Jensen, J. Kröger, R. Berndt, and S. Crampin, *Phys. Rev. B* **71**, 155417 (2005).
- [99] S. Crampin, H. Jensen, J. Kröger, L. Limot, and R. Berndt, *Phys. Rev. B* **72**, 035443 (2005).
- [100] B. N. Taber, C. F. Gervasi, J. M. Mills, D. A. Kislitsyn, E. R. Darzi, W. G. Crowley, R. Jasti, and G. V. Nazin, *J. Phys. Chem. Lett.* **7**, 3073 (2016).
- [101] K. Müller, M. Enache, and M. Stöhr, *J. Phys.: Condens. Matter* **28**, 153003 (2016).
- [102] L. Bürgi, O. Jeandupeux, A. Hirstein, H. Brune, and K. Kern, *Phys. Rev. Lett.* **81**, 5370 (1998).
- [103] A. Mugarza, A. Mascaraque, V. Pérez-Dieste, V. Repain, S. Rousset, F. J. García de Abajo, and J. E. Ortega, *Phys. Rev. Lett.* **87**, 107601 (2001).
- [104] A. Mugarza and J. E. Ortega, *Journal of Physics: Condensed Matter* **15**, S3281 (2003).
- [105] N. Zaki, K. Knox, P. D. Johnson, J. Fujii, I. Vobornik, G. Panaccione, and R. M. Osgood, *Phys. Rev. B* **83**, 205420 (2011).
- [106] S. K. Hämmäläinen, Z. Sun, M. P. Boneschanscher, A. Uppstu, M. Ijäs, A. Harju, D. Vanmaekelbergh, and P. Liljeroth, *Phys. Rev. Lett.* **107**, 236803 (2011).
- [107] S.-h. Phark, J. Borme, A. L. Vanegas, M. Corbetta, D. Sander, and J. Kirschner, *ACS Nano* **5**, 8162 (2011).

- 
- [108] S. J. Altenburg, J. Kröger, T. O. Wehling, B. Sachs, A. I. Lichtenstein, and R. Berndt, *Phys. Rev. Lett.* **108**, 206805 (2012).
- [109] D. Subramaniam, F. Libisch, Y. Li, C. Pauly, V. Geringer, R. Reiter, T. Mashoff, M. Liebmann, J. Burgdörfer, C. Busse, T. Michely, R. Mazzeo, M. Pratzner, and M. Morgenstern, *Phys. Rev. Lett.* **108**, 046801 (2012).
- [110] W. Jolie, F. Craes, M. Petrović, N. Atodiresei, V. Caciuc, S. Blügel, M. Kralj, T. Michely, and C. Busse, *Phys. Rev. B* **89**, 155435 (2014).
- [111] W. Jolie, F. Craes, and C. Busse, *Phys. Rev. B* **91**, 115419 (2015).
- [112] N. Nilius, T. M. Wallis, and W. Ho, *Science* **297**, 1853 (2002).
- [113] S. Fölsch, P. Hyldgaard, R. Koch, and K. H. Ploog, *Phys. Rev. Lett.* **92**, 056803 (2004).
- [114] S. Fölsch, J. Yang, C. Nacci, and K. Kanisawa, *Phys. Rev. Lett.* **103**, 096104 (2009).
- [115] J. Yang, C. Nacci, K. Kanisawa, and S. Fölsch, *J. Vac. Sci. Technol. B* **28**, C5G1 (2010).
- [116] E. H. Do and H. W. Yeom, *Phys. Rev. Lett.* **115**, 266803 (2015).
- [117] J. Repp, P. Liljeroth, and G. Meyer, *Nat. Phys.* **6**, 975 (2010).
- [118] S. Wang, W. Wang, and N. Lin, *Phys. Rev. Lett.* **106**, 206803 (2011).
- [119] S. R. Schofield, P. Studer, C. F. Hirjibehedin, N. J. Curson, G. Aeppli, and D. R. Bowler, *Nat. Commun.* **4**, 1649 (2013).
- [120] I. Swart, P. Liljeroth, and D. Vanmaekelbergh, *Chem. Rev.* **116**, 11181 (2016).
- [121] V. Lindberg and B. Hellsing, *J. Phys.: Condens. Matter* **17**, S1075 (2005).
- [122] W. Zhou and J. J. Coleman, *Curr. Opin. Solid State Mater. Sci.* **20**, 352 (2016).

- 
- [123] J. Mannhart, H. Boschker, T. Kopp, and R. Valentí, *Rep. Prog. Phys.* **79**, 084508 (2016).
- [124] G. Reecht, H. Bulou, F. Scheurer, V. Speisser, B. Carrière, F. Mathevet, and G. Schull, *Phys. Rev. Lett.* **110**, 056802 (2013).
- [125] Y. Zhao, J. Wyrick, F. D. Natterer, J. F. Rodriguez-Nieva, C. Lewandowski, K. Watanabe, T. Taniguchi, L. S. Levitov, N. B. Zhitenev, and J. A. Stroscio, *Science* **348**, 672 (2015).
- [126] O. Kurnosikov, D. V. Kulikov, V. S. Kharlamov, H. J. M. Swagten, and Yu. V. Trushin, *Phys. Rev. B* **84**, 054109 (2011).
- [127] O. Kurnosikov, J. H. Nietsch, M. Sicot, H. J. M. Swagten, and B. Koopmans, *Phys. Rev. Lett.* **102**, 066101 (2009).
- [128] O. Kurnosikov, H. J. M. Swagten, and B. Koopmans, *Phys. Rev. Lett.* **106**, 196803 (2011).
- [129] C. Sprodowski and K. Morgenstern, *Phys. Rev. B* **82**, 165444 (2010).
- [130] M. Müller, N. Néel, S. Crampin, and J. Kröger, *Phys. Rev. Lett.* **117**, 136803 (2016).
- [131] M. Schmid, S. Crampin, and P. Varga, *J. Electron Spectrosc. Relat. Phenom.* **109**, 71 (2000).
- [132] M. Hupalo and M. C. Tringides, *Phys. Rev. B* **65**, 115406 (2002).
- [133] R. Otero, A. L. Vázquez de Parga, and R. Miranda, *Phys. Rev. B* **66**, 115401 (2002).
- [134] M. Becker and R. Berndt, *Appl. Phys. Lett.* **96**, 033112 (2010).
- [135] M. Becker and R. Berndt, *Phys. Rev. B* **81**, 205438 (2010).
- [136] I.-P. Hong, C. Brun, F. Patthey, I. Y. Sklyadneva, X. Zubizarreta, R. Heid, V. M. Silkin, P. M. Echenique, K. P. Bohnen, E. V. Chulkov, and W.-D. Schneider, *Phys. Rev. B* **80**, 081409 (2009).



- 
- [137] J. E. Inglesfield, *The Embedding Method for Electronic Structure* (IOP Publishing, 2015).
- [138] J. Li, W.-D. Schneider, S. Crampin, and R. Berndt, *Surf. Sci.* **422**, 95 (1999).
- [139] J. H. Dil, T. U. Kampen, B. Hülsen, T. Seyller, and K. Horn, *Phys. Rev. B* **75**, 161401(R) (2007).
- [140] F. Yndurain and M. P. Jigato, *Phys. Rev. Lett.* **100**, 205501 (2008).



# List of the Author's Publications

## Complete List of Peer-Reviewed Journal Articles

1. M. Jahn, M. Müller, M. Endlich, N. Néel, J. Kröger, V. Chis, B. Hellsing  
*Oxygen vibrations and acoustic surface plasmon on Be(0001)*  
Phys. Rev. B **86**, 085453 (2012)  
DOI: 10.1103/PhysRevB.93.235402
2. M. Müller, C. Salgado, N. Néel, J. J. Palacios, J. Kröger  
*Plasticity of single-atom Pb junctions*  
Phys. Rev. B **93**, 235402 (2016)  
DOI: 10.1103/PhysRevB.86.085453
3. M. Müller, N. Néel, S. Crampin, J. Kröger  
*Lateral Electron Confinement with Open Boundaries: Quantum Well States above Nanocavities at Pb(111)*  
Phys. Rev. Lett. **117**, 136803 (2016)  
DOI: 10.1103/PhysRevLett.117.136803



# Erklärung

Ich versichere, dass ich die vorliegende Arbeit ohne unzulässige Hilfe Dritter und ohne Benutzung anderer als der angegebenen Hilfsmittel angefertigt habe. Die aus anderen Quellen direkt oder indirekt übernommenen Daten und Konzepte sind unter Angabe der Quelle gekennzeichnet.

Bei der Auswahl und Auswertung des vorgestellten Materials haben mir die nachstehend aufgeführten Personen in der jeweils beschriebenen Weise unentgeltlich geholfen:

1. Carlos Salgado und Prof. Dr. J. J. Palacios (Universidad Autónoma de Madrid) stellten DFT Rechnungen bereit, die zur Interpretation der experimentell gewonnen Leitwertkurven herangezogen wurden.
2. Dr. Simon Crampin (University of Bath) half mit seinen auf dem freien Elektronengas basierenden Simulationen der elektronischen Struktur im Volumen oberhalb vergrabener Vakanzen bei der Charakterisierung dieses neuartigen Einschlussmechanismus für Elektronen.
3. Dr. Nicolas Néel (Technische Universität Ilmenau) unterstützte mich bei der Interpretation der von mir aufgenommenen und ausgewerteten Messdaten sowie bei der Betreuung der Messapparatur.
4. Prof. Dr. Jörg Kröger (Technische Universität Ilmenau) unterstützte mich im Rahmen seiner Rolle als Fachgebietsleiter bei der Interpretation der von mir aufgenommenen und ausgewerteten Messdaten.

Weitere Personen waren an der inhaltlich-materiellen Erstellung der vorliegenden Arbeit nicht beteiligt. Insbesondere habe ich hierfür nicht die entgeltliche Hilfe von Vermittlungs- bzw. Beratungsdiensten (Promotionsberater oder anderer Personen) in Anspruch genommen. Niemand hat von mir unmittelbar oder

mittelbar geldwerte Leistungen für Arbeiten erhalten, die im Zusammenhang mit dem Inhalt der vorgelegten Dissertation stehen.

Die Arbeit wurde bisher weder im In- noch im Ausland in gleicher oder ähnlicher Form einer Prüfungsbehörde vorgelegt.

Ich bin darauf hingewiesen worden, dass die Unrichtigkeit der vorstehenden Erklärung als Täuschungsversuch bewertet wird und gemäß § 7 Abs. 10 der Promotionsordnung den Abbruch des Promotionsverfahrens zur Folge hat.

Ilmenau, 6. September 2017

---

Martin Müller

# Wissenschaftlicher Lebenslauf

## Persönliche Daten

Name: Martin Müller  
Geburtsdatum: 26.06.1989  
Geburtsort: Plauen

## Ausbildung

10/2013 – 08/2017 **Promotionsstudium**  
Institut für Physik, TU Ilmenau  
Promotionsstipendium der Carl-Zeiss-Stiftung  
Betreuer: Prof. Dr. Jörg Kröger

11/2011 – 10/2013 **Masterstudium Technische Physik**  
TU Ilmenau  
Thema Masterarbeit:  
*Leitwerte atomarer Kontakte auf Pb(111)*

10/2008 – 11/2011 **Bachelorstudium Technische Physik**  
TU Ilmenau  
Thema Bachelorarbeit:  
*Rastertunnelmikroskopische Untersuchungen an sauerstoffbedecktem Be(0001)-Kristall*

09/2000 – 07/2008 **Gymnasium**  
Diesterweg Gymnasium Plauen





# Danksagung

An dieser Stelle möchte ich mich bei allen Personen bedanken, die zum Gelingen dieser Arbeit beigetragen haben und mir stets mit Rat und Tat zur Seite standen.

Mein besonderer Dank gilt Prof. Dr. Jörg Kröger, der es mir ermöglichte meine Promotion im Fachgebiet Experimentalphysik 1 anzufertigen. Er war stets erreichbar für fachliche, sowie technische Fragen und gab zahlreiche Denkanstöße, die für die Interpretation der Ergebnisse von großer Bedeutung waren. Dr. Nicolas Néel danke ich für die Zusammenarbeit beim Betrieb der UHV-Anlage, sowie der Durchführung von Reparaturen und zahlreicher Optimierungen am experimentellen Aufbau und den vielen hilfreichen Diskussionen.

Carlos Salgado und Prof Dr. Juan Jose Palacios danke ich für die Bereitstellung von DFT Rechnungen, die bei der Interpretation der experimentellen Ergebnisse eine wichtige Rolle spielten. Dr. Simon Crampin danke ich für die Simulation der elektronischen Zustände in dünnen, lateral begrenzten Bleischichten, die neue Einblicke in die räumliche Beschränkung von Elektronen erlaubten.

Bei den restlichen aktuellen und ehemaligen Mitgliedern der Arbeitsgruppe möchte ich mich für die freundliche Arbeitsatmosphäre, die vielen hilfreichen Diskussionen, sowie der schnellen und unkomplizierten Hilfe bei größeren und kleineren Problemen bedanken: Jana Spindler, Sandra Gozdzik, Stefan Meierott, Michael Endlich, Jonathan Brand, Johannes Halle, Markus Girschik, Alexander Tries, Stefan Purle, Tobias Kreuch, Christian Günz, Sven Hoffmann, Marcel Rink und Gerd Hartung.

Prof. Dr. Stefan Krischok danke ich für seine Bereitschaft als Zweitgutachter für diese Arbeit zu agieren.

Der Fakultätswerkstatt danke ich für ihre schnelle und kompetente Hilfe bei verschiedensten Aufgaben. Auch spontane und besonders dringende Reparaturen oder Konstruktionen stellten nie ein Problem dar.

Besonderer Dank gilt auch meiner Lebensgefährtin Kristin, für ihre bedingungslose Unterstützung und ihrer Geduld in den letzten Monaten der Promotion.

Für die finanzielle Unterstützung bedanke ich mich insbesondere bei der Carl-Zeiss-Stiftung, die mit einem dreijährigen Promotionsstipendium die finanzielle Grundlage für diese Arbeit schuf.